The Astrophysical Journal, 897:148 (21pp), 2020 July 10 https://doi.org/10.3847/1538-4357/ab96c6

Verification of Radiative Transfer Schemes for the EHT

Roman Gold[1,2,3], Avery E. Broderick[3,4,5], Ziri Younsi[2,6], Christian M. Fromm[2], Charles F. Gammie[7], Monika Mościbrodzka[8], Hung-Yi Pu[3], Thomas Bronzwaer[8], Jordy Davelaar[8], Jason Dexter[9], David Ball[10], Chi-kwan Chan[10,11], Tomohisa Kawashima[12], Yosuke Mizuno[2], Bart Ripperda[13,14], Kazunori Akiyama[12,15,16,17], Antxon Alberdi[18], Walter Alef[19], Keiichi Asada[20], Rebecca Azulay[19,21,22], Anne-Kathrin Baczko[19], Mislav Baloković[17,23], John Barrett[16], Dan Bintley[24], Lindy Blackburn[17,23], Wilfred Boland[25], Katherine L. Bouman[17,23,26], Geoffrey C. Bower[27], Michael Bremer[28], Christiaan D. Brinkerink[8], Roger Brissenden[17,23], Silke Britzen[19], Dominique Broguiere[28], Do-Young Byun[29,30], John E. Carlstrom[31,32,33,34], Andrew Chael[35,107], Koushik Chatterjee[36], Shami Chatterjee[37], Ming-Tang Chen[27], Yongjun Chen (陈永军)[38,39], Ilje Cho[29,30], Pierre Christian[10,23], John E. Conway[40], James M. Cordes[37], Geoffrey B. Crew[16], Yuzhu Cui[41,42], Mariafelicia De Laurentis[2,43,44], Roger Deane[45,46], Jessica Dempsey[24], Gregory Desvignes[19,47], Sheperd S. Doeleman[17,23], Ralph?P. Eatough[19], Heino Falcke[8], Vincent L. Fish[16], Ed Fomalont[15], Raquel Fraga-Encinas[8], Bill Freeman[48,49], Per Friberg[24], José L. Gómez[18], Peter Galison[17,50,51], Roberto García[28], Olivier Gentaz[28], Boris Georgiev[4,5], Ciriaco Goddi[8,52], Minfeng Gu (顾敏峰)[38,53], Mark Gurwell[23], Kazuhiro Hada[41,42], Michael H. Hecht[16], Ronald Hesper[54], Luis C. Ho (何子山)[55,56], Paul Ho[20], Mareki Honma[41,42], Chih-Wei L. Huang[20], Lei Huang (黄磊)[38,53], David H. Hughes[57], Makoto Inoue[20], Sara Issaoun[8], David J. James[17,23], Buell T. Jannuzi[10], Michael Janssen[8], Britton Jeter[4], Wu Jiang (江悟)[38], Alejandra Jimenez-Rosales[58], Michael D. Johnson[17,23], Svetlana Jorstad[59,60], Taehyun Jung[29,30], Mansour Karami[3,61], Ramesh Karuppusamy[19], Garrett K. Keating[23], Mark Kettenis[62], Jae-Young Kim[19], Junhan Kim[10,26], Jongsoo Kim[29], Motoki Kino[12,63], Jun Yi Koay[20], Patrick M. Koch[20], Shoko Koyama[20], Michael Kramer[19], Carsten Kramer[28], Thomas P. Krichbaum[19], Cheng-Yu Kuo[64], Tod R. Lauer[65], Sang-Sung Lee[29], Yan-Rong Li (李彦荣)[66], Zhiyuan Li (李志远)[67,68], Rocco Lico[19], Michael Lindqvist[40], Kuo Liu[19], Elisabetta Liuzzo[69], Wen-Ping Lo[20,70], Andrei P. Lobanov[19], Laurent Loinard[71,72], Colin Lonsdale[16], Ru-Sen Lu (路如森)[19,38,39], Nicholas R. MacDonald[19], Sera Markoff[73], Jirong Mao (毛基荣)[74,75,76], Daniel P. Marrone[10], Alan P. Marscher[59], Iván Martí-Vidal[77], Satoki Matsushita[20], Lynn D. Matthews[16], Lia Medeiros[10,78], Karl M. Menten[19], Izumi Mizuno[24], James M. Moran[17,23], Kotaro Moriyama[41], Cornelia Müller[8,19], Hiroshi Nagai[79,80], Masanori Nakamura[20], Neil M. Nagar[81], Ramesh Narayan[17,23], Gopal Narayanan[82], Iniyan Natarajan[46], Roberto Neri[28], Chunchong Ni[4], Aristeidis Noutsos[19], Hiroki Okino[41,83], Gisela N. Ortiz-León[19], Tomoaki Oyama[41], Feryal Özel[10], Daniel C. M. Palumbo[17,23], Jongho Park[20], Nimesh Patel[23], Ue-Li Pen[3,84,85,86], Dominic W. Pesce[17,23], Richard Plambeck[87], Vincent Piétu[28], Aleksandar PopStefanija[82], Oliver Porth[2,36], Jorge A. Preciado-López[3], Dimitrios Psaltis[10], Venkatessh Ramakrishnan[81], Ramprasad Rao[27], Mark G. Rawlings[24], Alexander W. Raymond[17,23], Luciano Rezzolla[2,88], Freek Roelofs[8], Alan Rogers[16], Eduardo Ros[19], Mel Rose[10], Arash Roshanineshat[10], Helge Rottmann[19], Alan L. Roy[19], Chet Ruszczyk[16], Kazi L. J. Rygl[69], Salvador Sánchez[89], David Sánchez-Arguelles[57,90], Mahito Sasada[41,91], Tuomas Savolainen[19,92,93], Karl-Friedrich Schuster[28], F. Peter Schloerb[82], Lijing Shao[19,56], Zhiqiang Shen (沈志强)[38,39], Des Small[62], Bong Won Sohn[29,30,94], Jason SooHoo[16], Paul Tiede[3,4], Fumie Tazaki[41], Remo P. J. Tilanus[8,52,95], Michael Titus[16], Kenji Toma[96,97], Pablo Torne[19,89], Tyler Trent[10], Thalia Traianou[19], Sascha Trippe[98], Shuichiro Tsuda[99], Huib Jan van Langevelde[62,100], Ilse van Bemmel[62], Daniel R. van Rossum[8], Jan Wagner[19], John Wardle[101], Norbert Wex[19], Jonathan Weintroub[17,23], Robert Wharton[19], Maciek Wielgus[17,23], George N. Wong[102,103], Qingwen Wu (吴庆文)[104], Doosoo Yoon[36], Ken Young[23], André Young[8], Feng Yuan (袁峰)[38,53,105], Ye-Fei Yuan (袁业飞)[106], J. Anton Zensus[19], Guangyao Zhao[29], Shan-Shan Zhao[38], and Ziyan Zhu[51]

(The Event Horizon Telescope Collaboration)

[1] CP3-Origins, University of Southern Denmark, Campusvej 55, DK-5230 Odense M, Denmark; rg.roman.gold@gmail.com
[2] Institut für Theoretische Physik, Goethe-Universität Frankfurt, Max-von-Laue-Straße 1, D-60438 Frankfurt am Main, Germany
[3] Perimeter Institute for Theoretical Physics, 31 Caroline Street North, Waterloo, ON, N2L 2Y5, Canada
[4] Department of Physics and Astronomy, University of Waterloo, 200 University Avenue West, Waterloo, ON, N2L 3G1, Canada
[5] Waterloo Centre for Astrophysics, University of Waterloo, Waterloo, ON N2L 3G1, Canada
[6] Mullard Space Science Laboratory, University College London, Holmbury St. Mary, Dorking, Surrey, RH5 6NT, UK
[7] Department of Astronomy; Department of Physics; University of Illinois, Urbana, IL 61801, USA
[8] Department of Astrophysics, Institute for Mathematics, Astrophysics and Particle Physics (IMAPP), Radboud University, P.O. Box 9010, 6500 GL Nijmegen, The Netherlands
[9] JILA and Department of Astrophysical and Planetary Sciences, University of Colorado, Boulder, CO 80309, USA
[10] Steward Observatory and Department of Astronomy, University of Arizona, 933 N. Cherry Ave., Tucson, AZ 85721, USA
[11] Data Science Institute, University of Arizona, 1230 N. Cherry Ave., Tucson, AZ 85721, USA
[12] National Astronomical Observatory of Japan, 2-21-1 Osawa, Mitaka, Tokyo 181-8588, Japan
[13] Center for Computational Astrophysics, Flatiron Institute, 162 Fifth Avenue, New York, NY 10010, USA
[14] Department of Astrophysical Sciences, Peyton Hall, Princeton University, Princeton, NJ 08544, USA
[15] National Radio Astronomy Observatory, 520 Edgemont Rd, Charlottesville, VA 22903, USA
[16] Massachusetts Institute of Technology Haystack Observatory, 99 Millstone Road, Westford, MA 01886, USA
[17] Black Hole Initiative at Harvard University, 20 Garden Street, Cambridge, MA 02138, USA

[18] Instituto de Astrofísica de Andalucía—CSIC, Glorieta de la Astronomía s/n, E-18008 Granada, Spain
[19] Max-Planck-Institut für Radioastronomie, Auf dem Hügel 69, D-53121 Bonn, Germany; rlico@mpifr-bonn.mpg.de
[20] Institute of Astronomy and Astrophysics, Academia Sinica, 11F of Astronomy-Mathematics Building, AS/NTU No. 1, Sec. 4, Roosevelt Rd, Taipei 10617, Taiwan, R.O.C.
[21] Departament d'Astronomia i Astrofísica, Universitat de València, C. Dr. Moliner 50, E-46100 Burjassot, València, Spain
[22] Observatori Astronòmic, Universitat de València, C. Catedrático José Beltrán 2, E-46980 Paterna, València, Spain
[23] Center for Astrophysics | Harvard & Smithsonian, 60 Garden Street, Cambridge, MA 02138, USA
[24] East Asian Observatory, 660 N. A'ohoku Pl., Hilo, HI 96720, USA
[25] Nederlandse Onderzoekschool voor Astronomie (NOVA), P.O. Box 9513, 2300 RA Leiden, Niels Bohrweg 2, 2333 CA Leiden, The Netherlands
[26] California Institute of Technology, 1200 East California Boulevard, Pasadena, CA 91125, USA
[27] Institute of Astronomy and Astrophysics, Academia Sinica, 645 N. A'ohoku Place, Hilo, HI 96720, USA
[28] Institut de Radioastronomie Millimétrique, 300 rue de la Piscine, F-38406 Saint Martin d'Hères, France
[29] Korea Astronomy and Space Science Institute, Daedeok-daero 776, Yuseong-gu, Daejeon 34055, Republic of Korea
[30] University of Science and Technology, Gajeong-ro 217, Yuseong-gu, Daejeon 34113, Republic of Korea
[31] Kavli Institute for Cosmological Physics, University of Chicago, Chicago, IL 60637, USA
[32] Department of Astronomy and Astrophysics, University of Chicago, Chicago, IL 60637, USA
[33] Department of Physics, University of Chicago, Chicago, IL 60637, USA
[34] Enrico Fermi Institute, University of Chicago, Chicago, IL 60637, USA
[35] Princeton Center for Theoretical Science, Jadwin Hall, Princeton University, Princeton, NJ 08544, USA
[36] Anton Pannekoek Institute for Astronomy, University of Amsterdam, Science Park 904, 1098 XH, Amsterdam, The Netherlands
[37] Cornell Center for Astrophysics and Planetary Science, Cornell University, Ithaca, NY 14853, USA
[38] Shanghai Astronomical Observatory, Chinese Academy of Sciences, 80 Nandan Road, Shanghai 200030, People's Republic of China
[39] Key Laboratory of Radio Astronomy, Chinese Academy of Sciences, Nanjing 210008, People's Republic of China
[40] Department of Space, Earth and Environment, Chalmers University of Technology, Onsala Space Observatory, SE-439 92 Onsala, Sweden
[41] Mizusawa VLBI Observatory, National Astronomical Observatory of Japan, 2-12 Hoshigaoka, Mizusawa, Oshu, Iwate 023-0861, Japan
[42] Department of Astronomical Science, The Graduate University for Advanced Studies (SOKENDAI), 2-21-1 Osawa, Mitaka, Tokyo 181-8588, Japan
[43] Dipartimento di Fisica "E. Pancini," Universitá di Napoli "Federico II," Compl. Univ. di Monte S. Angelo, Edificio G, Via Cinthia, I-80126, Napoli, Italy
[44] INFN Sez. di Napoli, Compl. Univ. di Monte S. Angelo, Edificio G, Via Cinthia, I-80126, Napoli, Italy
[45] Department of Physics, University of Pretoria, Lynnwood Road, Hatfield, Pretoria 0083, South Africa
[46] Centre for Radio Astronomy Techniques and Technologies, Department of Physics and Electronics, Rhodes University, Grahamstown 6140, South Africa
[47] LESIA, Observatoire de Paris, Université PSL, CNRS, Sorbonne Université, Université de Paris, 5 place Jules Janssen, F-92195 Meudon, France
[48] Department of Electrical Engineering and Computer Science, Massachusetts Institute of Technology, 32-D476, 77 Massachussetts Ave., Cambridge, MA 02142, USA
[49] Google Research, 355 Main St., Cambridge, MA 02142, USA
[50] Department of History of Science, Harvard University, Cambridge, MA 02138, USA
[51] Department of Physics, Harvard University, Cambridge, MA 02138, USA
[52] Leiden Observatory-Allegro, Leiden University, P.O. Box 9513, 2300 RA Leiden, The Netherlands
[53] Key Laboratory for Research in Galaxies and Cosmology, Chinese Academy of Sciences, Shanghai 200030, People's Republic of China
[54] NOVA Sub-mm Instrumentation Group, Kapteyn Astronomical Institute, University of Groningen, Landleven 12, 9747 AD Groningen, The Netherlands
[55] Department of Astronomy, School of Physics, Peking University, Beijing 100871, People's Republic of China
[56] Kavli Institute for Astronomy and Astrophysics, Peking University, Beijing 100871, People's Republic of China
[57] Instituto Nacional de Astrofísica, Óptica y Electrónica. Apartado Postal 51 y 216, 72000. Puebla Pue., México
[58] Max-Planck-Institut für Extraterrestrische Physik, Giessenbachstr. 1, D-85748 Garching, Germany
[59] Institute for Astrophysical Research, Boston University, 725 Commonwealth Ave., Boston, MA 02215, USA
[60] Astronomical Institute, St.Petersburg University, Universitetskij pr., 28, Petrodvorets,198504 St.Petersburg, Russia
[61] University of Waterloo, 200 University Avenue West, Waterloo, Ontario N2L 3G1, Canada
[62] Joint Institute for VLBI ERIC (JIVE), Oude Hoogeveensedijk 4, 7991 PD Dwingeloo, The Netherlands
[63] Kogakuin University of Technology & Engineering, Academic Support Center, 2665-1 Nakano, Hachioji, Tokyo 192-0015, Japan
[64] Physics Department, National Sun Yat-Sen University, No. 70, Lien-Hai Rd, Kaosiung City 80424, Taiwan, R.O.C
[65] National Optical Astronomy Observatory, 950 North Cherry Ave., Tucson, AZ 85719, USA
[66] Key Laboratory for Particle Astrophysics, Institute of High Energy Physics, Chinese Academy of Sciences, 19B Yuquan Road, Shijingshan District, Beijing, People's Republic of China
[67] School of Astronomy and Space Science, Nanjing University, Nanjing 210023, People's Republic of China
[68] Key Laboratory of Modern Astronomy and Astrophysics, Nanjing University, Nanjing 210023, People's Republic of China
[69] Italian ALMA Regional Centre, INAF-Istituto di Radioastronomia, Via P. Gobetti 101, I-40129 Bologna, Italy
[70] Department of Physics, National Taiwan University, No.1, Sect. 4, Roosevelt Rd., Taipei 10617, Taiwan, R.O.C
[71] Instituto de Radioastronomía y Astrofísica, Universidad Nacional Autónoma de México, Morelia 58089, México
[72] Instituto de Astronomía, Universidad Nacional Autónoma de México, CdMx 04510, México
[73] Anton Pannekoek Institute for Astronomy & GRAPPA, University of Amsterdam, Postbus 94249, 1090GE Amsterdam, The Netherlands
[74] Yunnan Observatories, Chinese Academy of Sciences, 650011 Kunming, Yunnan Province, People's Republic of China
[75] Center for Astronomical Mega-Science, Chinese Academy of Sciences, 20A Datun Road, Chaoyang District, Beijing, 100012, People's Republic of China
[76] Key Laboratory for the Structure and Evolution of Celestial Objects, Chinese Academy of Sciences, 650011 Kunming, People's Republic of China
[77] Dpt. Astronomia i Astrofísica & Observatori Astronòmic (Universitat de València), Dr. Moliner 50, E-46100 Burjassot, València, Spain
[78] Department of Physics, Broida Hall, University of California Santa Barbara, Santa Barbara, CA 93106, USA
[79] National Astronomical Observatory of Japan, Osawa 2-21-1, Mitaka, Tokyo 181-8588, Japan
[80] Department of Astronomical Science, The Graduate University for Advanced Studies (SOKENDAI), Osawa 2-21-1, Mitaka, Tokyo 181-8588, Japan
[81] Astronomy Department, Universidad de Concepción, Casilla 160-C, Concepción, Chile
[82] Department of Astronomy, University of Massachusetts, 01003, Amherst, MA, USA
[83] Department of Astronomy, Graduate School of Science, The University of Tokyo, 7-3-1 Hongo, Bunkyo-ku, Tokyo 113-0033, Japan
[84] Canadian Institute for Theoretical Astrophysics, University of Toronto, 60 St. George Street, Toronto, ON M5S 3H8, Canada
[85] Dunlap Institute for Astronomy and Astrophysics, University of Toronto, 50 St. George Street, Toronto, ON M5S 3H4, Canada
[86] Canadian Institute for Advanced Research, 180 Dundas St West, Toronto, ON M5G 1Z8, Canada
[87] Radio Astronomy Laboratory, University of California, Berkeley, CA 94720, USA
[88] School of Mathematics, Trinity College, Dublin 2, Ireland
[89] Instituto de Radioastronomía Milimétrica, IRAM, Avenida Divina Pastora 7, Local 20, E-18012, Granada, Spain

[90] Consejo Nacional de Ciencia y Tecnología, Av. Insurgentes Sur 1582, 03940, Ciudad de México, México
[91] Hiroshima Astrophysical Science Center, Hiroshima University, 1-3-1 Kagamiyama, Higashi-Hiroshima, Hiroshima 739-8526, Japan
[92] Aalto University Department of Electronics and Nanoengineering, PL 15500, FI-00076 Aalto, Finland
[93] Aalto University Metsähovi Radio Observatory, Metsähovintie 114, FI-02540 Kylmälä, Finland
[94] Department of Astronomy, Yonsei University, Yonsei-ro 50, Seodaemun-gu, 03722 Seoul, Republic of Korea
[95] Netherlands Organisation for Scientific Research (NWO), Postbus 93138, 2509 AC Den Haag , The Netherlands
[96] Frontier Research Institute for Interdisciplinary Sciences, Tohoku University, Sendai 980-8578, Japan
[97] Astronomical Institute, Tohoku University, Sendai 980-8578, Japan
[98] Department of Physics and Astronomy, Seoul National University, Gwanak-gu, Seoul 08826, Republic of Korea
[99] Mizusawa VLBI Observatory, National Astronomical Observatory of Japan, Hoshigaoka 2-12, Mizusawa-ku, Oshu-shi, Iwate 023-0861, Japan
[100] Leiden Observatory, Leiden University, Postbus 2300, 9513 RA Leiden, The Netherlands
[101] Physics Department, Brandeis University, 415 South Street, Waltham, MA 02453, USA
[102] Department of Physics, University of Illinois, 1110 West Green St, Urbana, IL 61801, USA
[103] CCS-2, Los Alamos National Laboratory, P.O. Box 1663, Los Alamos, NM 87545, USA
[104] School of Physics, Huazhong University of Science and Technology, Wuhan, Hubei, 430074, People's Republic of China
[105] School of Astronomy and Space Sciences, University of Chinese Academy of Sciences, No. 19A Yuquan Road, Beijing 100049, People's Republic of China
[106] Astronomy Department, University of Science and Technology of China, Hefei 230026, People's Republic of China
Received 2020 January 15; revised 2020 May 19; accepted 2020 May 25; published 2020 July 13

Abstract

The Event Horizon Telescope (EHT) Collaboration has recently produced the first resolved images of the central supermassive black hole in the giant elliptical galaxy M87. Here we report on tests of the consistency and accuracy of the general relativistic radiative transfer codes used within the collaboration to model M87* and Sgr A*. We compare and evaluate (1) deflection angles for equatorial null geodesics in a Kerr spacetime; (2) images calculated from a series of simple, parameterized matter distributions in the Kerr metric using simplified emissivities and absorptivities; (3) for a subset of codes, images calculated from general relativistic magnetohydrodynamics simulations using different realistic synchrotron emissivities and absorptivities; (4) observables for the 2017 configuration of EHT, including visibility amplitudes and closure phases. The error in total flux is of order 1% when the codes are run with production numerical parameters. The dominant source of discrepancies for small camera distances is the location and detailed setup of the software "camera" that each code uses to produce synthetic images. We find that when numerical parameters are suitably chosen and the camera is sufficiently far away the images converge and that for given transfer coefficients, numerical uncertainties are unlikely to limit parameter estimation for the current generation of EHT observations. The purpose of this paper is to describe a verification and comparison of EHT radiative transfer codes. It is not to verify EHT models more generally.

Unified Astronomy Thesaurus concepts: Black hole physics (159); High energy astrophysics (739); Radiative transfer (1335); Relativity (1393); General relativity (641); Relativistic disks (1388); Very long baseline interferometry (1769); Radio astronomy (1338); Event horizons (479)

1. Introduction

The Event Horizon Telescope (EHT) is a millimeter-wavelength, Earth-sized very long baseline interferometry experiment that has recently imaged the shadow of the black hole (BH) in M87* at $\nu \simeq 230$ GHz (EHT Collaboration et al. 2019a, 2019b, 2019c, 2019d, 2019e, 2019f). The shadow is the gravitationally lensed image of the event horizon as seen by a distant observer. It is bounded by a ring of light emitted by hot plasma close to the event horizon. General relativity and other theories of gravity predict the angular size and shape of the shadow, which depends primarily on the BH's mass and distance. Using independent information about the distance, one can therefore determine the mass from a measurement of its angular size (EHT Collaboration et al. 2019d). Other features in the image are sensitive to astrophysical properties of the plasma near the BH.

The emitting plasma seen in EHT observations is brightest close to the BH (EHT Collaboration et al. 2019a, 2019b, 2019c, 2019d, 2019e, 2019f), where the deflection of light by the BH's gravitational field is strongest and where the speed of the emitting plasma v is close to the speed of light c. It is therefore required that models of EHT sources fully account for relativistic effects—those in both the matter dynamics and photon propagation.

Both M87* and Sgr A* accrete material at a rate significantly below the Eddington limit, and in most models the plasma is hot, magnetized, and turbulent (Yuan & Narayan 2014). Therefore, the most commonly used models for EHT sources such as Sgr A* and M87* incorporate a general relativistic magnetohydrodynamics (GRMHD) model for the flow of plasma close to the BH (EHT Collaboration et al. 2019f; Porth et al. 2019). The accuracy in these GRMHD studies has been investigated in great depth elsewhere (Porth et al. 2019). The resulting plasma is believed to emit primarily through the synchrotron process. Bremsstrahlung is negligible at energies below the X-ray. The optical depth to Thomson scattering in all models that we are aware of is small, $\lesssim 10^{-4}$, and scattering is therefore neglected in what follows; see also Thompson et al. (1994).[108] After assigning emission and absorption properties to the plasma obtained through the GRMHD simulation, one can produce a model total intensity image by solving the unpolarized radiative transport equations. Since there is no general analytic solution to the relativistic radiative transport equations, this requires a numerical solution.

[107] NASA Hubble Fellowship Program, Einstein Fellow.

[108] Notice that scattering can be important at wavelengths where synchrotron emission is weak.

The purpose of this paper is to verify that the codes used to create model images for the EHT accurately solve the equations of relativistic radiative transport[109] within the context of plasma models used in many previous single-fluid GRMHD simulations. It is not to verify EHT models more generally.

We quantify remaining discrepancies in the images via multiple metrics. First, we use the total flux and standard pixel-by-pixel based mean-square error (MSE) and the dissimilarity index (DSSIM). Second, we characterize errors in the visibility domain, specifically visibility amplitude (VA) and closure phase (CP), evaluated along baseline tracks relevant for the EHT.

Radiative transport is governed by the Boltzmann equation for photons. In sources where the light-crossing time is short compared with other timescales, $v/c \ll 1$, the gravitational potential $\phi/c^2 \ll 1$, and scattering is negligible, the Boltzmann equation for unpolarized photons can be reduced to the familiar form

$$\frac{dI_\nu}{ds} = j_\nu - \alpha_\nu I_\nu \tag{1}$$

(see, e.g., Rybicki & Lightman 2004). Here s is distance along a single ray or photon trajectory (which is a straight line), I_ν is the usual intensity (cgs units: erg cm^{-2} s^{-1} sr^{-1} Hz^{-1}), which is proportional to the photon phase space density, j_ν is the emissivity (cgs units: erg cm^{-3} s^{-1} sr^{-1} Hz^{-1}), and α_ν is the absorptivity (cgs units: cm^{-1}). The streaming or Liouville operator has been reduced to d/ds, and the terms on the right are a "collision operator" that describes interactions between photons and matter. Notice that one can solve this equation ray by ray, that is, beams of light propagating in different directions at a single point in space are decoupled because scattering is assumed absent.

A relativistic radiative transport equation can be obtained from the Boltzmann equation by expressing it in terms of frame-independent or invariant quantities (see Mihalas & Mihalas 1984; Rybicki & Lightman 2004 for a complete discussion). The photon phase space density is invariant and is proportional to I_ν/ν^3, as is j_ν/ν^2 and $\nu\alpha_\nu$. We use the affine parameter λ as the coordinate along a ray, with $ds \rightarrow \nu d\lambda$. Then the Boltzmann equation for unpolarized photons in the absence of scattering reduces to

$$\frac{d(I_\nu/\nu^3)}{d\lambda} = \left(\frac{j_\nu}{\nu^2}\right) - (\nu\alpha_\nu)\left(\frac{I_\nu}{\nu^3}\right). \tag{2}$$

Each quantity in parentheses is invariant and can be evaluated in any frame, although usually the transfer coefficients are specified in the plasma frame. The transfer coefficients j_ν, α_ν are now functions of λ. Frequency ν is frame dependent and a function of λ as well. Evidently, Equation (2) reduces to the nonrelativistic radiative transport equation if ν is independent of λ.

The problem is closed by specification of the photon trajectories. Each photon moves along a trajectory given by

$$\frac{dx^\mu}{d\lambda} = k^\mu, \tag{3}$$

where x^μ are the spacetime coordinates (for example, t, r, θ, ϕ in the usual Boyer–Lindquist coordinates for the Kerr metric) and k^μ is the photon wave four vector. In addition,

$$\frac{dk^\mu}{d\lambda} = -\Gamma^\mu_{\alpha\beta} k^\alpha k^\beta, \tag{4}$$

where Γ is the connection, which depends on the metric. The metric is arbitrary; no assumption needs to be made about whether the metric is a solution to Einstein's equations. However, all tests presented here will adopt the Kerr metric.

The algorithms tested here typically form images as follows. Each pixel on the image corresponds to a wavevector. The corresponding geodesic is traced backward toward the BH, ending either close to the horizon or when the geodesic escapes again to a large distance from the hole. The geodesic trajectory is recorded, and the radiative transfer equation is integrated forward along it. The result is a final value of Stokes I_ν at a point in each pixel. The flux density in each pixel can be estimated as $F_\nu \approx I_\nu \Delta\Omega$, where $\Delta\Omega$ is the solid angle subtended by the pixel.

This paper is organized as follows. Section 2 provides a list and description of participating codes. Section 3 describes a sequence of tests, which includes a test of the geodesic integration as well as comparisons of images formed from an analytically specified model, which allows for an exact comparison and clear dissection of error sources. Section 5 describes results of the test set and shows good agreement between the various codes. Section 5.4 describes results of a more advanced and realistic comparison between two pairs of codes on sample GRMHD-generated data. Section 6 lists the main caveats, and Section 7 presents the conclusions.

2. Codes

Below we describe 10 general relativistic radiative transfer codes. The first is a `Mathematica` code that is capable of solving the problem to arbitrary precision and that can therefore provide a reference solution. The remainder are (in alphabetical order) `BHOSS`, `GRay`, `GRay2`, `GRTRANS`, `IPOLE`, `ODYSSEY`, `RAIKOU`, `RAPTOR`, and `VRT2`.

Out of these, `BHOSS`, `IPOLE`, `RAPTOR`, and `GRTRANS` are coupled to the EHT parameter estimation framework `THEMIS` (Broderick et al. 2020) via a driver routine, while `VRT2` and `ODYSSEY` are both natively included.

2.1. Stand-Alone `Mathematica` Code

All ingredients in the image tests presented in Section 3 are analytic, as opposed to being specified in terms of interpolated quantities from a GRMHD simulation. In addition the metric and connection are also analytic. Given analytic emissivities and absorptivities, one can then in principle calculate the solution exactly. Motivated by this we have written a stand-alone `Mathematica` script that can solve the basic equations to any desired precision, that is, using arbitrary precision floating point arithmetic.

This stand-alone code is based on the formulation of `BHOSS` (described below), integrating the geodesic equations of motion and the decoupled radiative transfer equation simultaneously. As such, the next position on the geodesic, four-momentum, intensity, and optical depth are determined at every integration step. The integration itself is performed using a standard Runge–Kutta–Fehlberg scheme with

[109] Note that many separate modeling efforts within the EHT do not involve the computation of theoretical images.

adaptive step sizing. If the error in the geodesic properties, the intensity, or optical depth is too large, then the integration is repeated at a smaller step size such that the error remains within a prespecified tolerance.

Since Mathematica can perform calculations using arbitrary precision arithmetic, one can specify the number of digits of precision sought in a calculation. In all subsequent calculations with the stand-alone code we demand 16 digits of precision so that each ray's intensity and optical depth is accurate to double precision. We refer to results from this code as EXACT.

2.2. BHOSS

The BHOSS code (Younsi et al. 2020) performs geodesic integration and general-relativistic radiative transfer in arbitrary coordinate systems and arbitrary spacetime metrics (e.g., Younsi et al. 2016) to machine precision using a variety of numerical schemes. Polarized radiative transfer and nonvacuum GRMHD data have been developed and tested in Younsi et al. (2020). Many accretion flow models commonly used in the literature are included, as are many emission and absorption coefficients using different distribution functions (and physical assumptions in their derivation). Additional models, emission, absorption coefficients, and so on are easily incorporated due to the modular nature of the code. BHOSS interfaces to the output of BHAC (Porth et al. 2017), 2D and 3D variants of HARM (Gammie et al. 2003; Noble et al. 2009), and H-AMR (Liska et al. 2018; Chatterjee et al. 2019) GRMHD codes.

2.3. GRay and GRay2

GRay is a massively parallel ordinary differential equation integrator (Chan et al. 2013). It employs the stream processing paradigm and runs on NVIDIA's graphics processing units (GPUs). It is designed to efficiently integrate null geodesics in curved spacetime according to Einstein's general theory of relativity and efficiently solve the radiative transfer equations. It uses the NVIDIA CUDA platform and is written in CUDA/C. Hence, it requires NVIDIA's GPUs. When it was first developed (mainly in 2012 and 2013), the code performed about 30 times faster than similar codes running on CPUs. The code was used in an extensive image parameter study (Chan et al. 2015a) and a time-variability study (Chan et al. 2015b) of Sgr A*.

GRAY2 is a massively parallel geodesic integrator for performing general relativistic ray-tracing and radiative transfer (GRRT) for accreting BHs (Chan et al. 2018). It is based on the lux framework https://github.com/luxsrc and uses OpenCL to achieve portable performance on a wide range of modern hardware/accelerators such as GPUs and Intel® Xeon Phi.

One major improvement of GRAY2 over GRAY is that, instead of using the Boyer–Lindquist coordinates, the geodesic equations are integrated in the Cartesian Kerr–Schild coordinates. The algorithm turns out to be conceptually more straightforward and easier to understand. Although this method does not take advantage of symmetry of the Kerr spacetime, we found a method to reformulate the geodesic equations so that it outperforms Boyer–Lindquist coordinates on modern GPUs. In addition, the coordinate singularity at the event horizon that is present in Boyer–Lindquist coordinates is avoided.

2.4. GRTRANS

The GRTRANS code[110] (Dexter 2016) solves the polarized radiative transfer equations along rays (null geodesics) in a Kerr spacetime. Geodesics are calculated using the GEOKERR code (Dexter & Agol 2009). The radiative transfer equations are integrated either numerically (Hindmarsch 2007) or with quadrature methods (Landi Degl'Innocenti 1985; Rees et al. 1989). Both methods are used for the tests described here.

Fluid and emission models are defined in separate modules. Examples include different forms of synchrotron emission and fluid models ranging from semianalytic models like those used as test problems here to postprocessing of time-dependent, 2D and 3D GRMHD simulation data in particular from codes based on HARM (Gammie et al. 2003; Noble et al. 2006).

2.5. IPOLE

IPOLE (Mościbrodzka & Gammie 2018) is a covariant ray-tracing radiative transfer code capable of integrating the fully polarized synchrotron radiative transfer problem in arbitrary spacetime and arbitrary coordinates. The code extends the IBOTHROS scheme (Noble et al. 2007) for unpolarized transport. IPOLE uses a second-order null geodesic integrator, and radiative transfer equations are solved along geodesics using an analytic solution to the polarized transport equation with constant transfer coefficients (Landi Degl'Innocenti 1985). In a fiducial setup, the code operates in the Kerr–Schild metric, but alternative metrics are straightforward to implement. The code is interfaced with GRMHD simulations produced by a HARM3D code, and it is parallelized with openMP. Using simple (plasma in a slab) and complicated model problems (an accretion disk around a Kerr BH), IPOLE produces Stokes parameters or polarization maps that converge to those produced by GRTRANS (see Section 2.4). IPOLE is consistent with IBOTHROS and has additionally been checked against the Monte Carlo GRRT scheme grmonty (Dolence et al. 2009). IPOLE is publicly available.[111]

2.6. ODYSSEY

Written in CUDA (Compute Unified Device Architecture) C/C++, ODYSSEY[112] (Pu et al. 2016b) is a GPU-based, public code for radiative transfer in curved spacetime, based on the ray-tracing algorithm in Fuerst & Wu (2004) and the radiative transfer formula in Younsi et al. (2012). ODYSSEY performs radiative transfer for unpolarized thermal and nonthermal synchrotron emission (Pu et al. 2016a). An extension of ODYSSEY with a polarized GRRT scheme for thermal synchrotron emission is described in Pu & Broderick (2018).

2.7. RAIKOU (来光)

RAIKOU (来光) (see Kawashima et al. 2019 for an application of the code), is a general relativistic ray-tracing radiative transfer code in which the cyclo-synchrotron emission/absorption for thermal/nonthermal electrons, bremsstrahlung emission/absorption, and Compton/inverse-Compton scattering are implemented. The null geodesic equations are integrated by solving Hamilton's canonical equations of motion

[110] Publicly available at https://github.com/jadexter/grtrans.
[111] Publicly available at https://github.com/moscibrodzka/ipole.
[112] Publicly available at https://github.com/hungyipu/Odyssey.

describing the time evolution of r, θ, ϕ, p_r, p_θ of photons in Boyer–Lindquist coordinates. The solver performing the ray tracing is based on an eighth-order embedded Runge–Kutta method with the adaptive step-size control.

The radiative transfer equation for synchrotron and bremsstrahlung are then solved by tracing these null rays from the observer to the emitter, ignoring effects due to Comptonization. For solving the transfer equation including Compton/inverse-Compton scattering, a Monte Carlo method is used, and here the photons are traced from the emitter to the observer.

2.8. RAPTOR

RAPTOR[113] (Bronzwaer et al. 2018) constructs synthetic images of accreting BHs by performing time-dependent radiative transfer along null geodesics, in arbitrary spacetimes. The null geodesics are constructed by solving the geodesic equation for light rays using a second-order (Verlet) or a second- or fourth-order (Runge–Kutta) integrator. Radiative transfer calculations are performed "backward" along the rays, as they are constructed, for efficiency. The code is written in C and may be compiled and executed on both CPUs and GPUs via the OpenACC framework. It includes emission coefficients for thermal as well as nonthermal (κ-distribution; Davelaar et al. 2018b) synchrotron radiation. RAPTOR accepts GRMHD output data from BHAC (Porth et al. 2017; uniform and nonuniform [AMR] grids Davelaar et al. 2019), HARM2D, and HARM3D (Gammie et al. 2003; Noble et al. 2009). RAPTOR is also capable of producing full-sky images, which are used to create virtual reality animations (Davelaar et al. 2018a).

2.9. VRT2

VRT2 is based on the plasma radiative transfer package described in Broderick & Blandford (2003, 2004). It provides a modular framework for adding novel plasma distributions, radiative transfer mechanisms, and spacetime structures. In particular, it formed the basis for the images generated in, for example, Broderick et al. (2011) and used in the analysis of Broderick et al. (2016).

3. Tests

3.1. Pure Ray-tracing Test

A necessary but not sufficient condition for verification of general relativistic, radiative transfer codes is a correct computation of photon paths in the underlying spacetime.

As a first test we consider the computation of null geodesics in a highly spinning Kerr BH, and in particular the deflection angles for light rays as a function of their impact parameter b. The deflection angle can be obtained via quadrature of standard, elliptic functions (Iyer & Hansen 2009) to arbitrary accuracy for photons moving in the equatorial plane of the BH. Closed-form expressions for arbitrarily inclined geodesics are provided by Gralla & Lupsasca (2020).

3.2. Analytic Model Image Tests

We now consider a set of analytically specified models. In order to generate an image, one must specify a spacetime and an emissivity and absorptivity on the spacetime. Since the emissivity and absorptivity are frame dependent, we must also specify a four-velocity for the frame in which they are defined. In what follows, we assume the Kerr metric and specialize to Boyer–Lindquist coordinates t, r, θ, ϕ. We adopt geometrical units with $G = c = \hbar = 1$, so that all length and timescales are given in terms of the BH mass M. All of the models are assumed to be time independent.

Emissivities and absorptivities are given in the comoving frame of the fluid. The inclination of the source with respect to the distant observer is fixed at $i = 60°$ (relative to polar/BH spin axis). The BH mass is fixed to $M = 6 \times 10^{11}\,\mathrm{cm} \sim 4 \times 10^6 M_\odot$, and the source distance is $d = 2.4 \times 10^{22}\,\mathrm{cm} \sim 7.78\,\mathrm{kpc}$.

All models can be described as follows.

The number density of the fluid is

$$n = n_0 \exp\left\{-\frac{1}{2}\left[\left(\frac{r}{10}\right)^2 + z^2\right]\right\}, \tag{5}$$

where $z \equiv h\cos\theta$ and n_0 is a reference number density. Here h is used to control the vertical scale height.

The angular momentum profile is

$$l = \left(\frac{l_0}{1+R}\right) R^{1+q}, \tag{6}$$

where $R \equiv r\sin\theta$ and $q = 0.5$. The covariant fluid four-velocity is thus

$$u_\mu = \bar{u}(-1, 0, 0, l), \tag{7}$$

where

$$\bar{u} = \sqrt{-(g^{tt} - 2g^{t\phi}l + g^{\phi\phi}l^2)^{-1}}, \tag{8}$$

so that $u_\mu u^\mu = -1$.

The fluid emissivity is

$$j_\nu = Cn\left(\frac{\nu}{\nu_p}\right)^{-\alpha}, \tag{9}$$

where C is a constant. We set the combination $Cn_0 = 3 \times 10^{-18}\,\mathrm{erg\,cm^{-3}\,s^{-1}\,sr^{-1}\,Hz^{-1}}$. Notice that ν is expressed in units of the pivotal frequency $\nu_\mathrm{p} = 230\,\mathrm{GHz}$. The invariant emissivity is

$$j_\mathrm{inv} = \frac{j_\nu}{\nu^2}. \tag{10}$$

The absorptivity of the fluid is

$$\alpha_\nu = A\,C\,n\left(\frac{\nu}{\nu_p}\right)^{-(\beta+\alpha)}, \tag{11}$$

where $\beta = 2.5$. The source function in the tests with absorption (tests 4 and 5) is given by $S_\nu = (j_\nu/\alpha_\nu) = (\nu/\nu_p)^\beta/A$. The absorptivity unit is $\mathrm{cm^{-1}}$. The Lorentz-invariant absorptivity then reads as

$$\alpha_\mathrm{inv} = \nu\,\alpha_\nu. \tag{12}$$

Finally, the dimensionless spin parameter $a \equiv J/M^2$, where J is the total ADM (Arnowitt–Deser–Misner) angular momentum and M is the total (ADM) mass of the BH spacetime.

The free parameters in the test are therefore a, A, α, h, l_0, which are explicitly specified in Table 1. All rays are traced until they are either within $10^{-4}M$ of the BH event horizon or

[113] Publicly available at https://github.com/tbronzwaer/raptor.

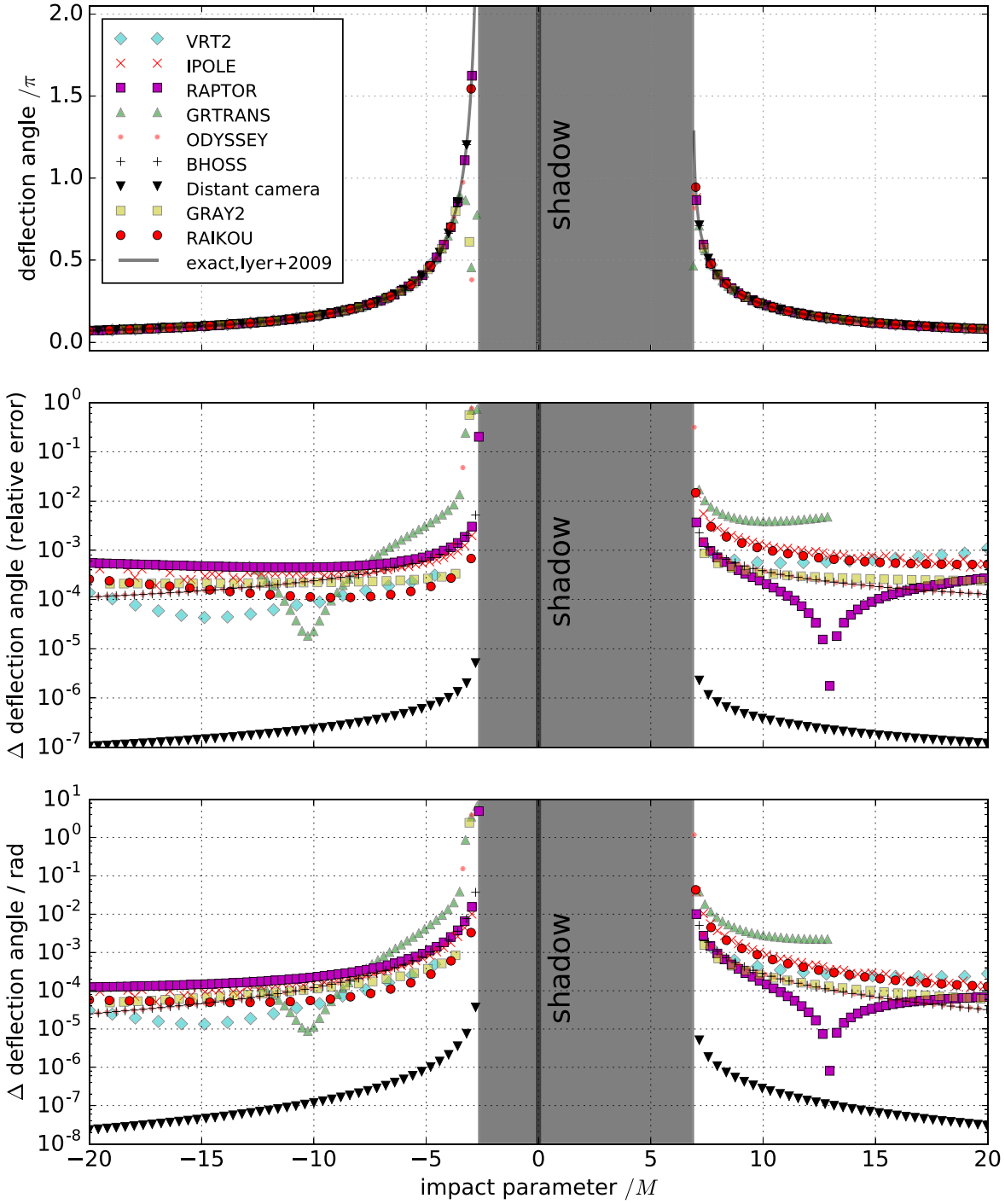

Figure 1. Results of former geodesic integration test in the equatorial plane in the Kerr geometry for eight different codes. Results are compared to an exact solution. Remaining residuals are due to finite camera position. For reference, the results for a more distant camera position are shown from the BHOSS code. The detailed test setup is not described here.

Table 1
List of Parameter Values Defining the Standardized Imaging Tests

Test	A	α	h	l_0	a
1	0	−3	0	0	0.9
2	0	−2	0	1	0
3	0	0	10/3	1	0.9
4	10^5	0	10/3	1	0.9
5	10^6	0	100/3	1	0.9

have "escaped" the BH beyond the coordinate distance of the camera.

To summarize, the five parameters in the standardized imaging tests and their meaning are

1. A: controls the degree of absorption of the fluid
2. α: controls the frequency dependence of the fluid emissivity and consequently also the absorptivity
3. h: controls the scale-height of the accretion disk and therefore the vertical concentration of matter within the fluid

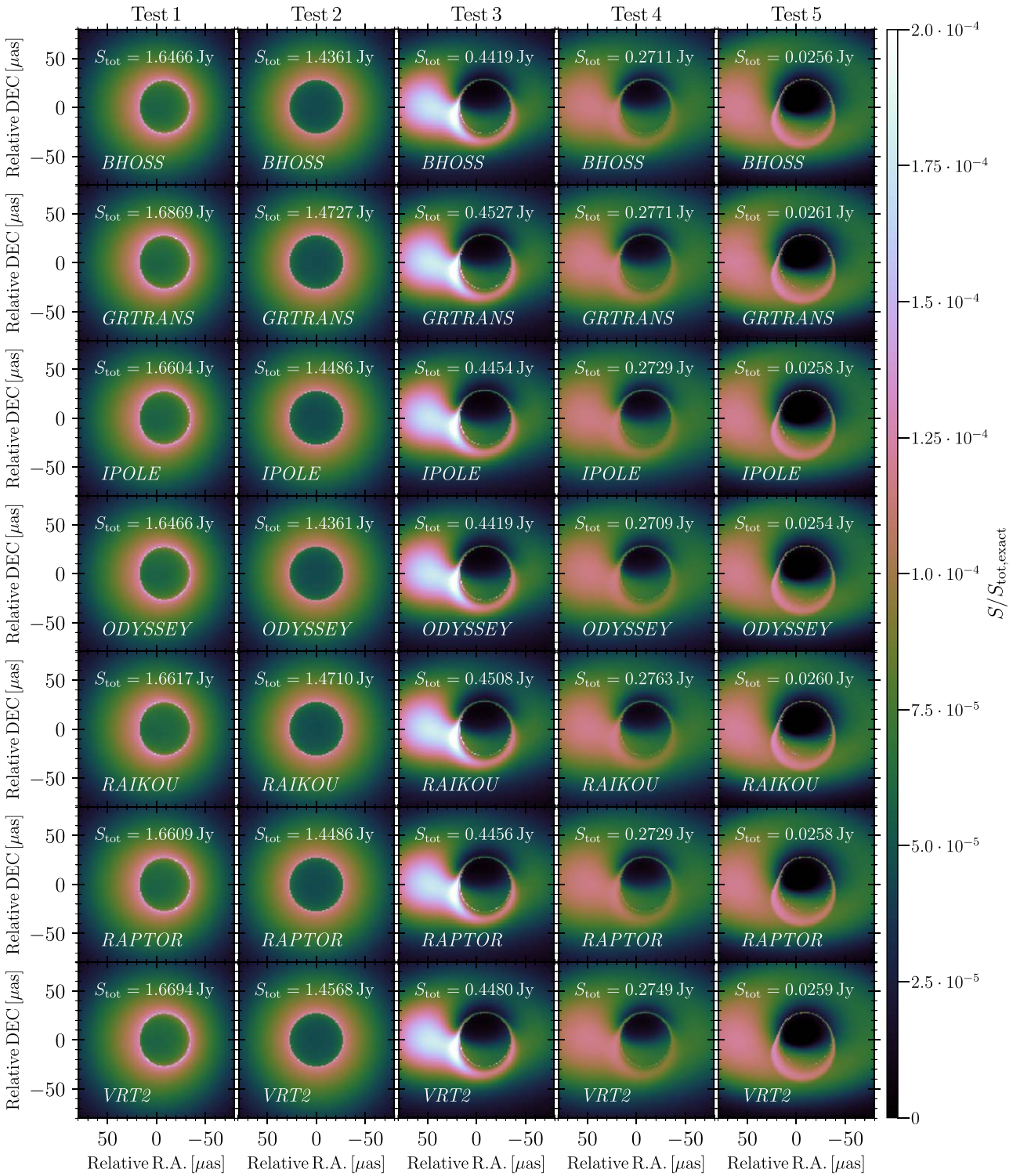

Figure 2. Images of the proposed test cases obtained with different codes (from top to bottom) BHOSS, GRTRANS, IPOLE/IBOTHROS, ODYSSEY, RAIKOU (来光), RAPTOR, and VRT2 with the total flux $S_{\rm tot}$ shown in each panel. The images have been normalized to the total flux of the exact solution. West (on the sky) is to the right. The field of view ranges from $-15M$ to $+15M$, where M is the gravitational radius ($r_g = GM/c^2$). The resolution is 128 × 128 pixels.

4. l_0: specifies whether the fluid is rotating ($l_0 = 1$) or purely radially infalling ($l_0 = 0$)
5. a: sets the spin of the BH

We compare code performance on five tests.

Test 1 features a spinning BH surrounded by a nonrotating matter distribution with no vertical structure and no absorption. The spectral index $\alpha = -3$ essentially corresponds to the computation of the column density. In the image the asymmetry is caused by the spacetime only.

In test 2, a nonrotating BH, surrounded by a matter distribution with pseudo-Keplerian rotation is assumed. The spectral index $\alpha = -2$ corresponds to the Rayleigh–Jeans limit of a thermal gas and exactly (emissivity $\propto \nu^2$) compensates Doppler beaming due to flow rotation. As a result of this

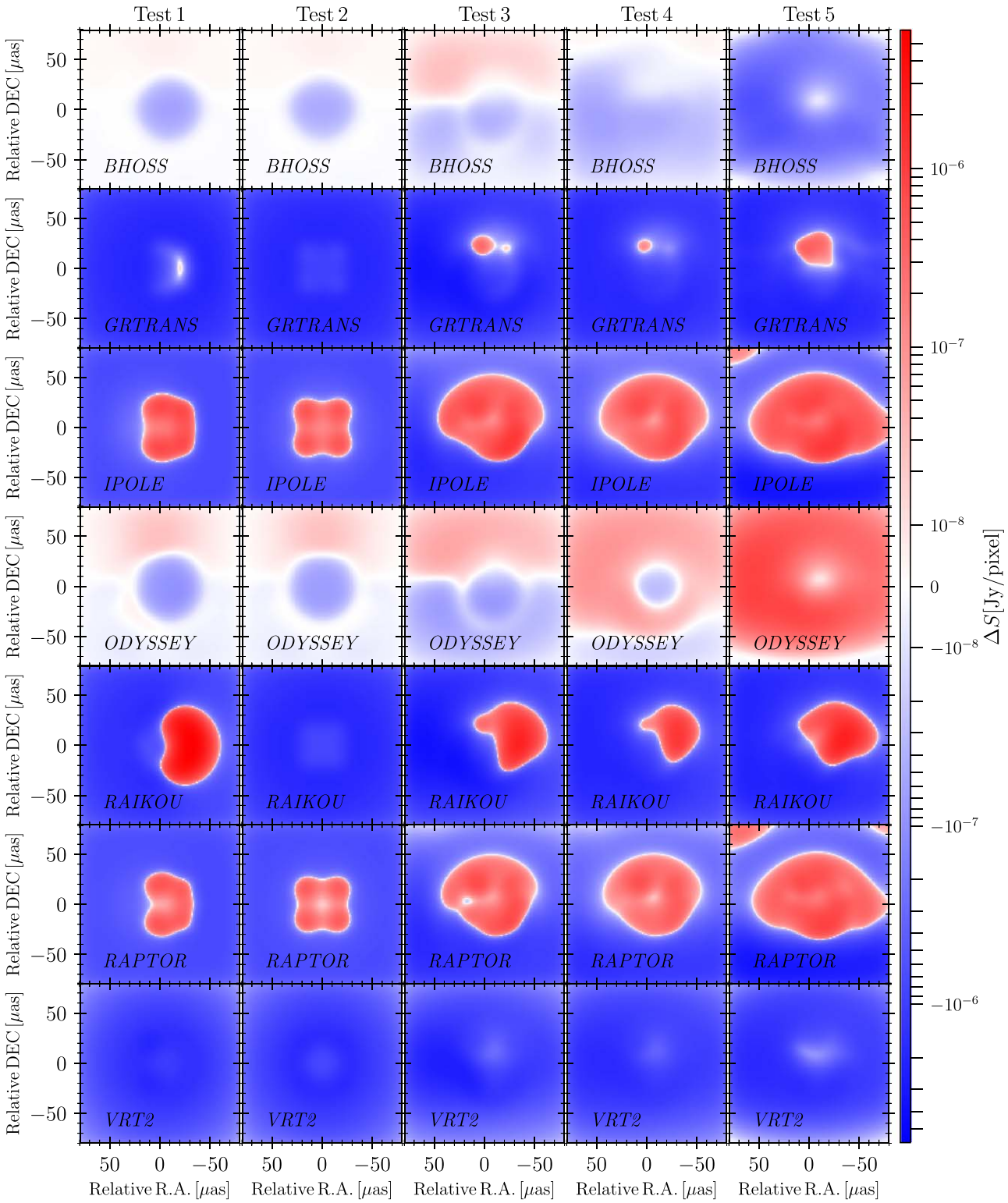

Figure 3. Difference images of the proposed test cases showing differences to the exact solution in janskys after convolving with the beam for different codes (from top to bottom) BHOSS, GRTRANS, IPOLE/IBOTHROS, ODYSSEY, RAIKOU (来光), RAPTOR, and VRT2. White represents perfect agreement, blue indicates lower, and red indicates higher flux than the exact solution.

delicate balance, the image of test 2 appears spherically symmetric in a nontrivial way.

In tests 3–5, a graybody ($\alpha = 0$) emission is assumed. With fixed disk height h between tests 3 and 4, the optically thin case ($A = 0$, test 3) has a larger total flux than the case with absorption ($A \neq 0$, cases 4). Tests 4 and 5 probe different levels of absorption and different disk scale heights.

Finally, a technical point related to image production. We found that most code authors had made different choices for forming the image, that is, for the software *camera*. This commonly led to different image scales, centering, and rotation.

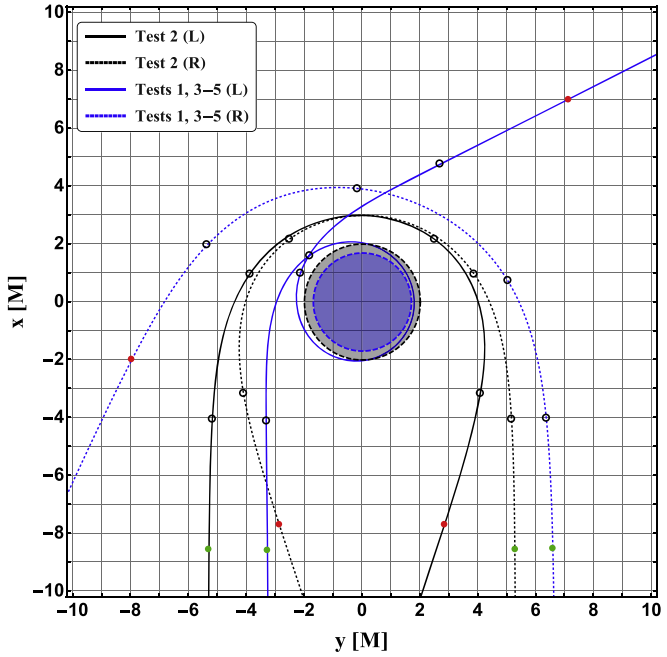

Figure 4. Equatorial trajectories of rays that come closest to the BH and still escape, either to the left (solid curves) or to the right (dotted curves) of the BH itself. The observer camera setup is identical to that specified in the radiative transfer tests. For the Schwarzschild BH ($a = 0$, black curves, test 2), the grid indices of the α impact parameter (not to be confused with the spectral index used later) are 42 and 87 (out of 128), for the left and right rays, respectively. Similarly, for the $a = 0.9$ case (tests 1, 3, 4, and 5), the left and right grid indices are 51 and 93, respectively. The event horizons of the BHs are denoted by the shaded gray and blue circles with dashed edges, respectively. Overlaid circles indicate equidistant values of the affine parameter along the ray and are placed at $\lambda = (990, 995, 1000, 1005, 1010, 1015)$ for each of the four geodesics. Filled green circles denote $\lambda = 990$ (when the ray approaches the BH), and filled red circles denote $\lambda = 1015$ (when the ray departs the BH). Unfilled black circles denote values of $\lambda = 995$, 1000, 1005, and 1010 between the green and red filled circles. See text for further discussion.

Table 2
Total Fluxes for Tests 1–5 for All Participating Codes

Code	Test 1	Test 2	Test 3	Test 4	Test 5
EXACT	1.6465	1.4360	0.4418	0.2710	0.0255
BHOSS	1.6466	1.4361	0.4419	0.2711	0.0256
GRTRANS	1.6606	1.4498	0.4457	0.2727	0.0257
IPOLE	1.6604	1.4486	0.4454	0.2729	0.0258
ODYSSEY	1.6466	1.4361	0.4419	0.2709	0.0254
RAIKOU	1.6617	1.4710	0.4508	0.2763	0.0260
RAPTOR	1.6609	1.4486	0.4456	0.2729	0.0258
VRT2	1.6694	1.4568	0.4480	0.2749	0.0259

Note. All fluxes are in units of janskys.

In the standardized tests, we place the camera at a finite distance, 1000 M, from the BH. The camera has a field of view of $30M \times 30M$, with the BH spin axis projecting onto the up direction in the image plane. The camera is assumed stationary ($u^r = 0$) in Boyer–Lindquist coordinates. It is pointed so that photons that arrive at the center of the image have zero angular momentum ($k_\phi = 0$).

Table 3
MSE and DSSIM for Images from Tests 1–5 for All Participating Codes

Code	Test	MSE	DSSIM
BHOSS	1	1.7011e−06	2.1887e−07
	2	1.3944e−06	1.2326e−07
	3	1.8660e−06	8.8399e−08
	4	3.2655e−06	1.7919e−07
	5	2.9300e−05	1.2812e−05
GRTRANS	1	1.8911e−04	8.2037e−04
	2	1.9279e−04	5.9234e−04
	3	2.0637e−04	5.9093e−04
	4	1.7044e−04	4.8334e−04
	5	1.7945e−04	6.5113e−04
IPOLE	1	7.4251e−05	3.3934e−04
	2	7.2089e−05	2.3235e−04
	3	1.0195e−04	4.1756e−04
	4	8.6420e−05	3.4324e−04
	5	1.6414e−04	1.4359e−03
ODYSSEY	1	2.9380e−06	7.4417e−07
	2	2.3575e−06	3.8843e−07
	3	4.0151e−06	4.2490e−07
	4	5.5067e−06	7.4341e−07
	5	5.1753e−05	3.9980e−05
RAIKOU	1	1.8079e−04	2.8168e−03
	2	1.8581e−04	5.1424e−04
	3	2.0885e−04	7.2374e−04
	4	1.6491e−04	6.1596e−04
	5	1.7901e−04	9.1854e−04
RAPTOR	1	7.1418e−05	2.6176e−04
	2	7.0195e−05	2.1199e−04
	3	9.5067e−05	3.3171e−04
	4	8.0648e−05	2.7717e−04
	5	1.5354e−04	1.2289e−03
VRT2	1	1.2048e−04	2.1074e−04
	2	1.2375e−04	2.7119e−04
	3	1.2981e−04	1.6993e−04
	4	1.2073e−04	1.9027e−04
	5	1.2318e−04	2.0244e−04

Note. No attempt was made to optimize the results of this comparison. Instead, these results were obtained with standard choices for certain numerical parameters (such as error tolerance, limiting distance to the horizon up to which rays are traced, etc.) for each code. Such inhomogeneities in the comparison can cause deviations. Therefore these numbers present only conservative estimates for the ultimate achievable accuracy with each code.

4. Methods

4.1. Image Fidelity Metrics

We compare two images adopting two image-comparison metrics: the MSE and the DSSIM (Lu et al. 2016), which were also used, for example, in Mizuno et al. (2018) and can be computed as

$$\mathrm{MSE} := \frac{\sum_{j=1}^{N} |I_j - K_j|^2}{\sum_{j=1}^{N} |I_j|^2} \tag{13}$$

$$\mathrm{SSIM}(I, K) := \left(\frac{2\mu_I \mu_K}{\mu_I^2 + \mu_K^2}\right)\left(\frac{2\sigma_{IK}}{\sigma_I^2 + \sigma_K^2}\right) \tag{14}$$

$$\mathrm{DSSIM}(I, K) := 1/|\mathrm{SSIM}| - 1, \tag{15}$$

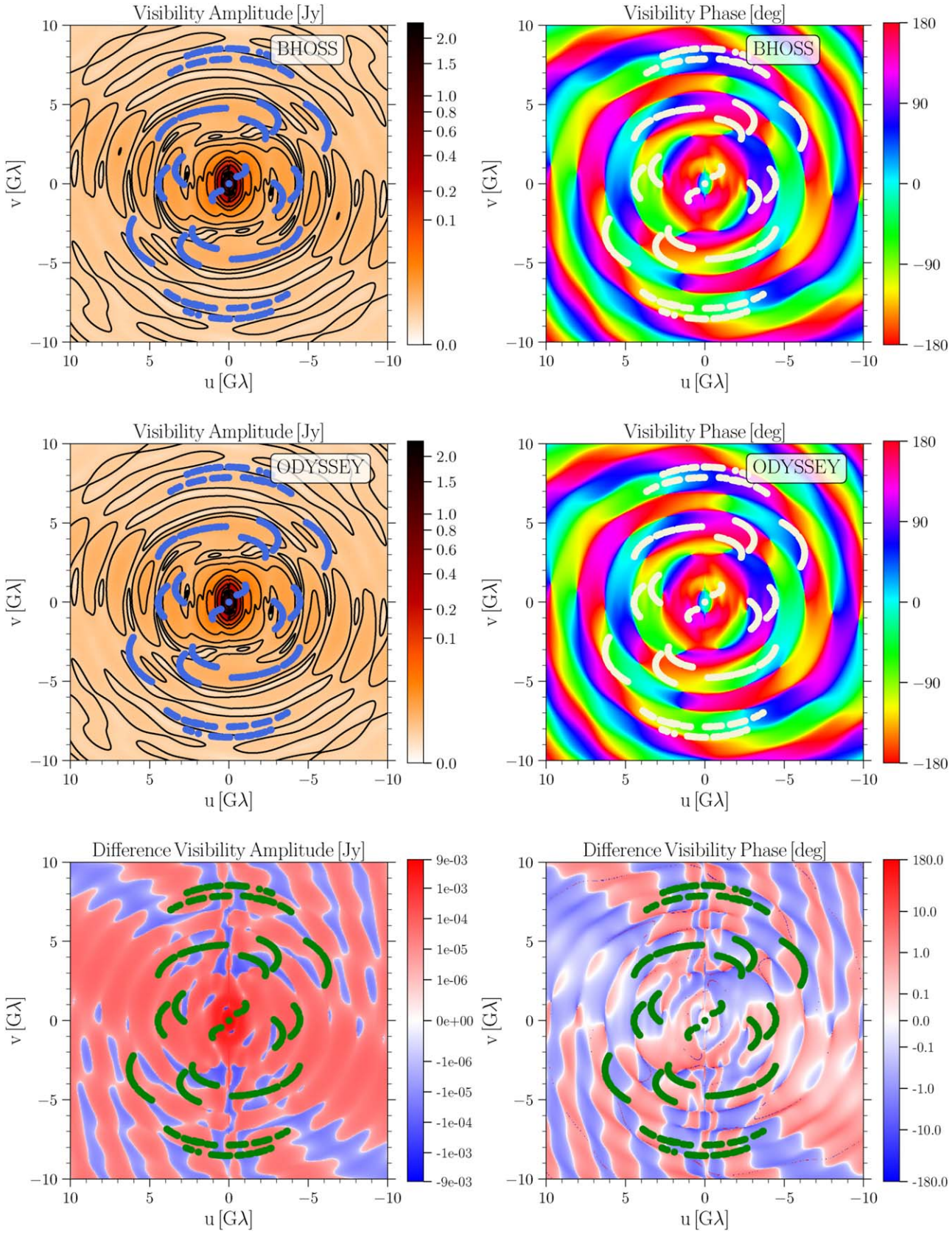

Figure 5. Intrinsic VAs and CPs for standardized imaging test 5 as generated from the images obtained by `BHOSS` and `Odyssey`. The blue/white/green dots show the *uv* coordinates probed by an EHT 2017 configuration for Sgr A*. The color bar ranges for the differences are symmetrical logarithmic with a linear threshold set to 0.05.

Table 4
Deviations from the Exact Solution Produced by the Various Codes for the Five Standardized Image Tests as Measured by the Median Deviation of Simulated VA and CP Data

Code	Test	Median (VA) (Jy)	Median (CP) (deg)
BHOSS	1	5.6694e−06	1.6345e−02
	2	5.7606e−06	2.0285e−02
	3	6.8076e−06	2.2161e−02
	4	2.0204e−06	2.9291e−02
	5	3.0713e−05	2.7993e−01
GRTRANS	1	3.8645e−04	3.4847e+00
	2	2.4088e−04	4.5702e−03
	3	2.5688e−04	9.8301e−01
	4	1.5970e−04	2.3652e+00
	5	3.4818e−04	1.6285e+00
IPOLE	1	3.4597e−04	1.1569e+00
	2	1.9036e−04	1.8315e−02
	3	2.6388e−04	1.4334e+00
	4	1.4109e−04	2.4776e+00
	5	3.9559e−04	2.0832e+00
ODYSSEY	1	1.3080e−05	4.1182e−02
	2	1.0429e−05	5.9483e−02
	3	2.0955e−05	7.4016e−02
	4	1.4011e−05	2.8735e−01
	5	8.1137e−05	5.5927e−01
RAIKOU	1	8.2747e−04	1.1019e+01
	2	2.3538e−04	1.5799e−02
	3	2.3431e−04	1.6306e+00
	4	1.3102e−04	2.4126e+00
	5	2.4376e−04	2.1510e+00
RAPTOR	1	3.3082e−04	1.4639e+00
	2	1.7456e−04	2.0506e−02
	3	2.8488e−04	1.2109e+00
	4	1.4605e−04	2.3062e+00
	5	3.7217e−04	1.9362e+00
VRT2	1	2.6217e−04	7.5180e−01
	2	3.6318e−04	8.9474e−03
	3	3.7755e−04	1.9007e−01
	4	1.7589e−04	7.7138e−01
	5	2.0798e−04	8.6086e−01

Note. All VA deviations are well within observational uncertainties even on baselines including ALMA, and CP deviations are mostly smaller than uncertainties on CP measurements except for very few cases where they are comparable. This indicates that for these idealized test settings, code discrepancies are subdominant over observational uncertainties under the assumption that we know what equations to solve.

where $\mu_I \coloneqq \sum_{i=1}^{N} I_i/N$, $\sigma_I^2 \coloneqq \sum_{j=1}^{N}(I_j - \mu_j)^2/(N-1)$, $\sigma_{IK} \coloneqq \sum_{j-1}^{N}(I_j - \mu_I)(K_j - \mu_K)/(N-1)$, and I_j and K_j are the intensities of two images at pixel j. Note that for two identical images MSE = DSSIM = 0 and SSIM = 1.

5. Results

5.1. Ray-tracing Test: Deflection Angle in Kerr Geometry

In Figure 1 we summarize the results of the purely geodesic deflection angle test in the equatorial plane of a Kerr BH performed by eight radiative transfer codes: IPOLE, ODYSSEY, VRT2, GRTRANS, GRAY2, BHOSS, RAPTOR, and RAIKOU (来光). The gray solid line shows the exact results computed following Iyer & Hansen (2009). Good agreement of all codes is evident. Deviations are largest very close to the horizons where deflection angles can even exceed 2π and sensitivity to initial data becomes exponential. The slight discrepancy at larger radii of order 10^{-4} is due to the finite starting point of the geodesics compared to the infinite distance assumed for the exact expression. We have separately verified that the limiting factor is the finite distance of the camera to the source. Evidently, finite accuracy in the computations of geodesics is not a limiting factor in model predictions.

5.2. Imaging Tests

We move on to imaging tests that in addition to ray tracing also involve solving the radiative transfer equation along null geodesics. Image models that are highly simplified are useful to characterize basic image features but are ultimately limited in their applicability to sources like M87*; see, for example, Nalewajko et al. (2020). On the other end, GRMHD-inspired models can have a very complex structure that complicates interpretation and verification.

In this section we describe tests that strike a good balance between the two former types. These tests involve several aspects and image features that are qualitatively similar to more realistic GRMHD-inspired models but are much simpler in many respects. We are most interested in understanding the results from each code for typical numerical parameters to simulate realistic/computationally feasible conditions. This also means that any discrepancies found here are not an indication of the ultimate accuracy of any one code.

The results of the five standardized imaging tests, presented in Section 4, for IPOLE/IBOTHROS, BHOSS, GRTRANS, ODYSSEY, RAIKOU (来光), RAPTOR, and VRT2 are shown in Figures 2 and 3. In terms of total flux the relative discrepancies among all codes are ∼0.6% or less; see Table 2. The only regions where images differ by eye are isolated pixels near the light ring. A quantitative analysis reveals smaller differences. Again as in the geodesic test in the previous subsection, the remaining discrepancies are dominated by the finite distance of the camera to the source and the finite field of view.

Figure 4 presents reference geodesics of rays that comprise test 2 (black curves) and tests 1, 3, 4 and 5 (blue curves), which differ in the BH spin, as indicated in Table 1. Horizontal and vertical impact parameters (α and β, respectively) are as defined in the deflection angle test. Rays that come closest to the BH while still escaping (i.e., that comprise the shadow boundary) come within closer proximity to the event horizon of the BH in the $a = 0.9$ case (blue curves).

The corresponding values for MSE and DSSIM are summarized in Table 3. Clearly, the images from all codes are very similar for each test according to these metrics. However, we will see in Section 5.3, where we compare using simulated data for each code, that such image-based metrics can give a misleading impression of the similarity for observational or model-fitting purposes.

In Section 5.4, we also present an analysis of tests involving more complex image structures involving GRMHD snapshots.

5.3. Quantifying Relevance for Parameter Estimation: Simulated Data

As a first step toward characterizing the importance or possible limitations due to finite accuracy of radiative transfer

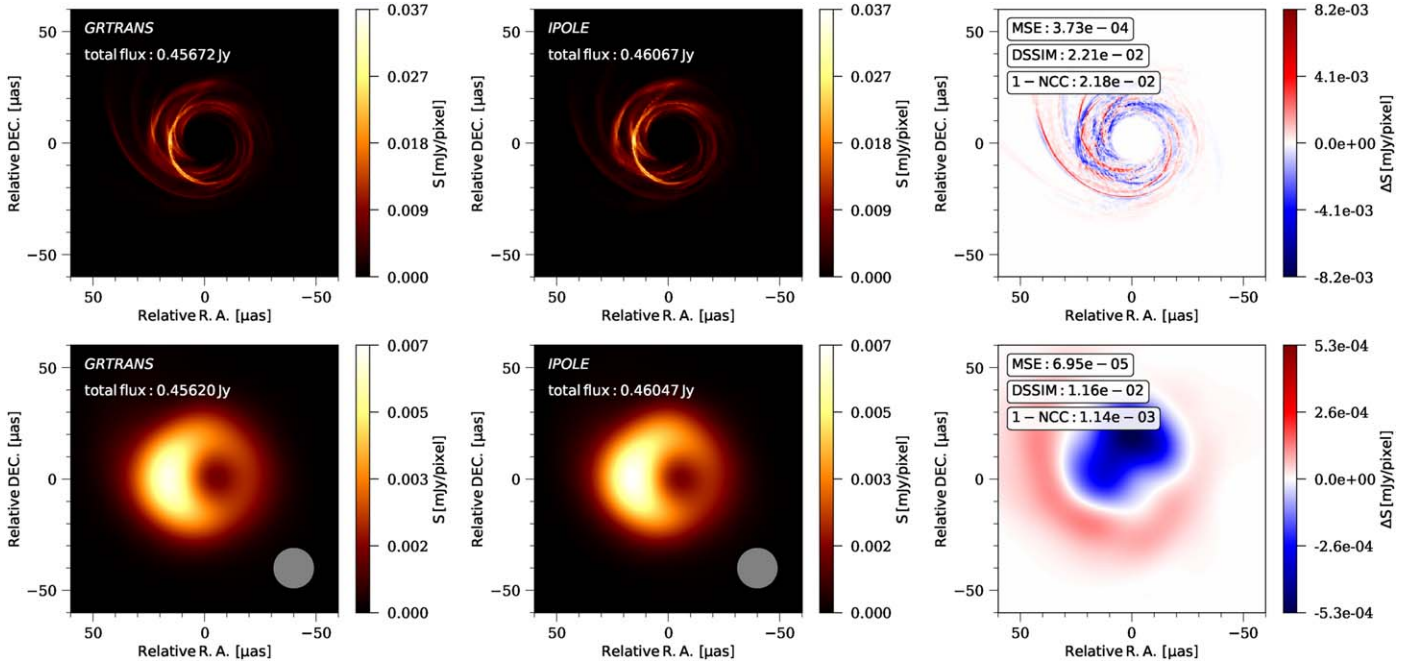

Figure 6. Model images of the BH and the jet launching point in M87 core produced by GRTRANS and IPOLE based on the same snapshot of a 3D GRMHD simulation of an accreting BH. The model is taken from Mościbrodzka et al. (2016) (model RH100 in their Table 1).

schemes on model fitting and parameter estimation we use the EHT-im library (Chael et al. 2016, 2018) to simulate realistic VA and CP data including realistic error bars for a typical set of parameters for a Sgr A* observation with a 2017 array configuration (results are quite similar for an M87* coverage). We also refer to Figure 5, which shows the intrinsic VA, CP, and their differences for BHOSS and ODYSSEY for test 5.

The near zero baseline $u = v \sim 0$ (e.g., JCMT-SMA or ALMA-APEX) simulated data are spuriously affected by the small field of view in the model images and have therefore been excluded from the analysis. Note that the large-scale structure probed by the short baselines is the regime where the ray tracing and radiative transfer are most accurate, so omitting these regions from the test is justified. We have tested separately with a subset of codes that the agreement between codes improves further when we increase the field of view (in particular to the fields of view used in EHT Collaboration et al. 2019d, 2019f).

We also rescale the flux in all tests to 1 Jy before computing simulated data similar to the flux levels measured in M87* and not far away from those measured in Sgr A*.

We compute the differences in VA and CP for each code relative to the ones obtained from the exact solution and report the median in Table 4. The differences in VA are always much smaller than observational uncertainties. Differences in CP can be crudely compared to a systematic error in CP of $\sim 2°$ as was determined for the recent M87* observation. Most codes for most tests produce smaller errors than the observational uncertainties, and the exceptions are more marginal.

We acknowledge that the model images used for the standardized imaging tests are simpler than GRMHD-inspired model images or the EHT 2017 data set of M87*. As a result many additional contributions to the error budget in more realistic model images are not included here. However, this analysis nevertheless gives an indication of the error budget under the idealized assumption that the equations solved and prescriptions adopted are sufficient to describe the system.

Next we consider additional, more realistic image tests with more complex structure involving GRMHD data, albeit for a subset of codes used in the previous section.

5.4. Comparison of Images from a Full GRMHD Model

Ultimately the spatial structure and time-dependent behavior seen in the synchrotron emission of the main science targets for the EHT are determined by solutions to the equations of GRMHD. Three-dimensional global simulations are of great use in the context of interpreting EHT data (EHT Collaboration et al. 2019d, 2019f; Porth et al. 2019). The fact that image models are often informed by GRMHD simulations means that they will inherit some of the uncertainties reported in Porth et al. (2019). Here we show side-by-side code comparisons involving such GRMHD-based radiative models. These comparisons are substantially more challenging than the standardized image tests due to the more complex image structure and the true relativistic synchrotron emissivities being nonanalytic (Leung et al. 2011).

Comparison between IPOLE and GRTRANS. The first comparison of a more advanced test involving radiative transfer of a 3D GRMHD simulation snapshot is based on data obtained by the HARM3D code. Two radiative transfer codes presented in Section 2 used on the same GRMHD simulation snapshot, namely, GRTRANS and IBOTHROS (a former intensity-only version of IPOLE), were used with the same parameters and with the same synchrotron emissivity functions. The obtained intrinsic model images are shown for comparison in Figure 6 and give an excellent indication of how small the differences due to finite accuracy in the radiative transfer and ray tracing are. Figure 6 shows a model image of the M87 jet launching point as observed at $f = 230$ GHz. The jet model is taken from Mościbrodzka et al. (2016) (see model

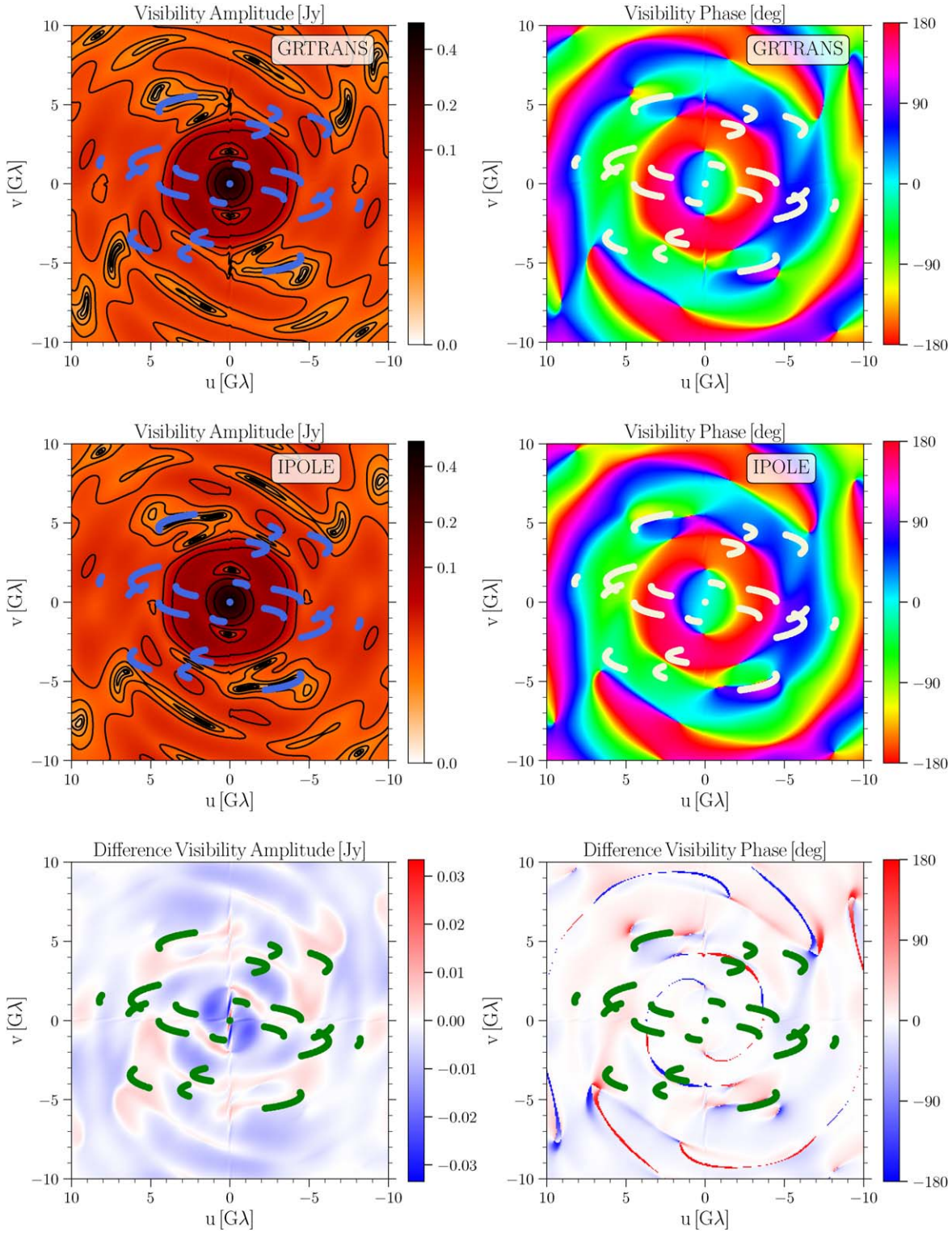

Figure 7. Intrinsic VAs and CPs for the full GRMHD comparison between GRTRANS and IPOLE. The blue dots show the *uv* coordinates probed by an EHT 2017 configuration for M87*.

RH100 in their Table 1 for all model parameter details). The viewing angle is $i = 20°$, and the total flux at this frequency is 1 Jy.

As before for the standardized imaging test 5, we present the intrinsic VA, CP, and their differences, but for the full GRMHD comparison between GRTRANS and IPOLE in Figure 7.

Comparison between RAPTOR and BHOSS. The second comparison, between RAPTOR and BHOSS, also uses a turbulent 3D GRMHD snapshot obtained from BHAC. Identical synchrotron emissivities based on the relativistic Maxwell–Jüttner distribution were employed, and all other observer and setup parameters were fixed to be equal in both codes. The resulting images can be seen in Figure 8; see also

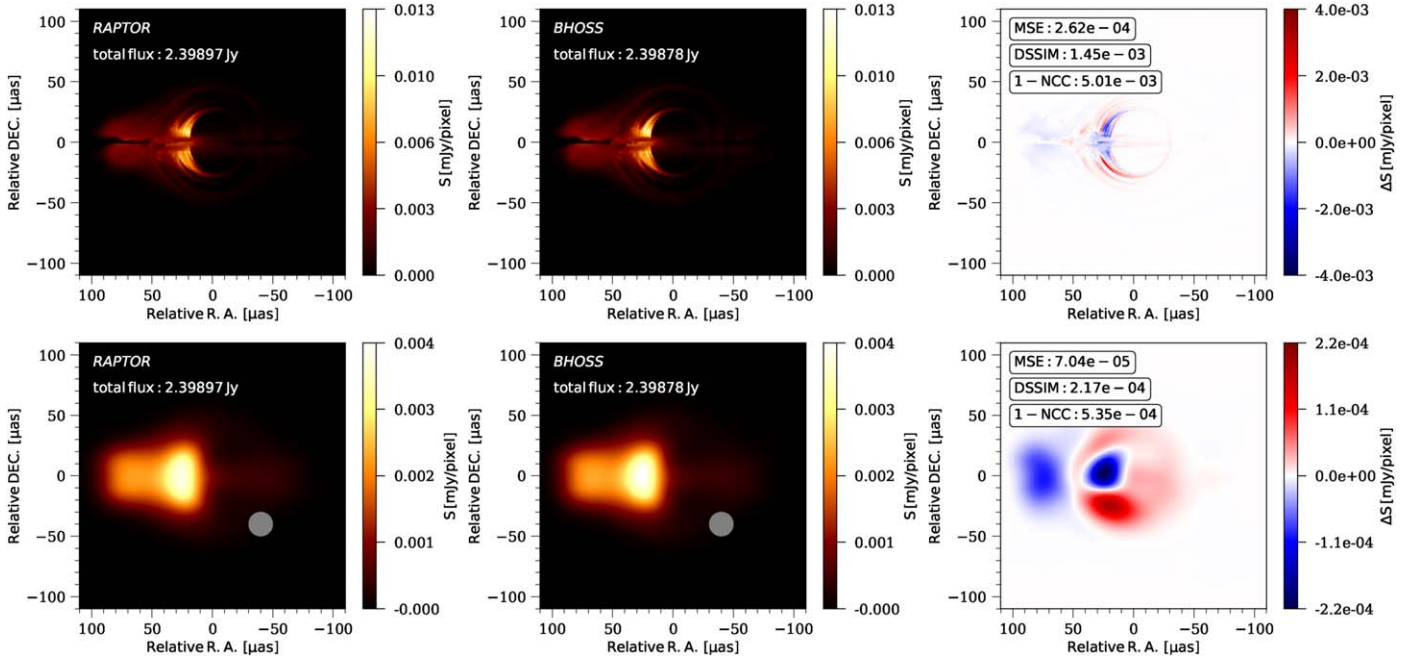

Figure 8. Results of an image comparison between BHOSS and RAPTOR featuring a full GRMHD model. The test setup is not described here.

Bronzwaer et al. (2018). Again, the differences between the two codes are visibly small, and it was found that differences in total flux between both images decreased with increasing image resolution. The largest pixel-to-pixel differences were observed in (1) regions of very low (effectively floor) density and (2) regions very close to the event horizon, where differences in geodesic integration and step size strategies were found to lead to nonnegligible differences in the gravitational redshift, giving rise to more pronounced differences in the pixel fluxes (see Figure 6 for more details).

The chosen inclination for this test was 90°, that is, viewed edge on along the equatorial plane. This angle was chosen to provide the strongest test of gravitational lensing. At a resolution of 4096 × 4096 pixels, the total image fluxes from RAPTOR and BHOSS were 2.39896 Jy and 2.39881 Jy, respectively, that is, a relative difference of 0.06%.

As before for the standardized imaging test 5, we present the intrinsic VA, CP, and their differences, but for the full GRMHD comparison between BHOSS and RAPTOR in Figure 9.

Together with the deflection angle test, the standardized imaging test, and the full GRMHD tests presented here, these results suggest that all image discrepancies across all tests are small and that the standardized imaging tests broadly capture the main discrepant features.

5.5. Synchrotron Emissivities

We also investigated the influence of different choices for the synchrotron emissivity on the simulated data by using GRTRANS on the same GRMHD snapshot (but different from the previous snapshots) using three different synchrotron emissivities: approximate Θ-dependent emissivities (Θ is the "pitch" angle, that is, the angle between the photon wavevector k and the local magnetic field) using fitting functions from (1) Mahadevan et al. (1996), (2) symphony (Pandya et al. 2016), and (3) a Θ-averaged expression.

The result of this comparison shows that all three synchrotron emissivities give VA data discrepancies of 1.2×10^{-3} Jy (two Θ-dependent fitting functions) and 2.7×10^{-2} Jy (Θ-dependent versus Θ-averaged). These differences are smaller than observational uncertainties and would therefore be indistinguishable with an EHT 2017 configuration. Discrepancies due to Θ-averaging can be marginal, however, and are for this model visible in the emission size and dim side in the image domain; see Figure 10.

For the CP data we find similarly insignificant median deviations, 0.27°, between the two Θ-dependent emissivities, but a large median discrepancy 11.3° between Θ-dependent and Θ-averaged.

This analysis highlights that the usage of angle-averaged emissivities in generating models for EHT observations is discouraged and either full or symphony emissivities should be used in order to avoid significant parameter estimation biases.

This aspect needs to be reevaluated in the context of a larger variety of source models and especially polarized emissivities, which can be more sensitive to such differences than the intensity-only emissivities considered here.

6. Caveats

In this work we compare several radiative transfer codes on a single standardized, albeit idealized, testing scheme. The standardized (and stationary) imaging tests feature a much smoother and simpler matter distribution than the real data or more realistic models. All tests presented are limited to unpolarized radiation. The tests are restricted to the Kerr solution of GR. In all tests, a single thermal distribution function for the relativistic electrons is assumed. We focus on situations where the source is not exhibiting flares. The measured total flux alone considerably narrows down the range of relevant densities.The standardized (and stationary) imaging tests use a simple prescription for the emissivity that ignore other potentially complicating factors, known from more realistic treatments, such as uncertainties due to interpolations

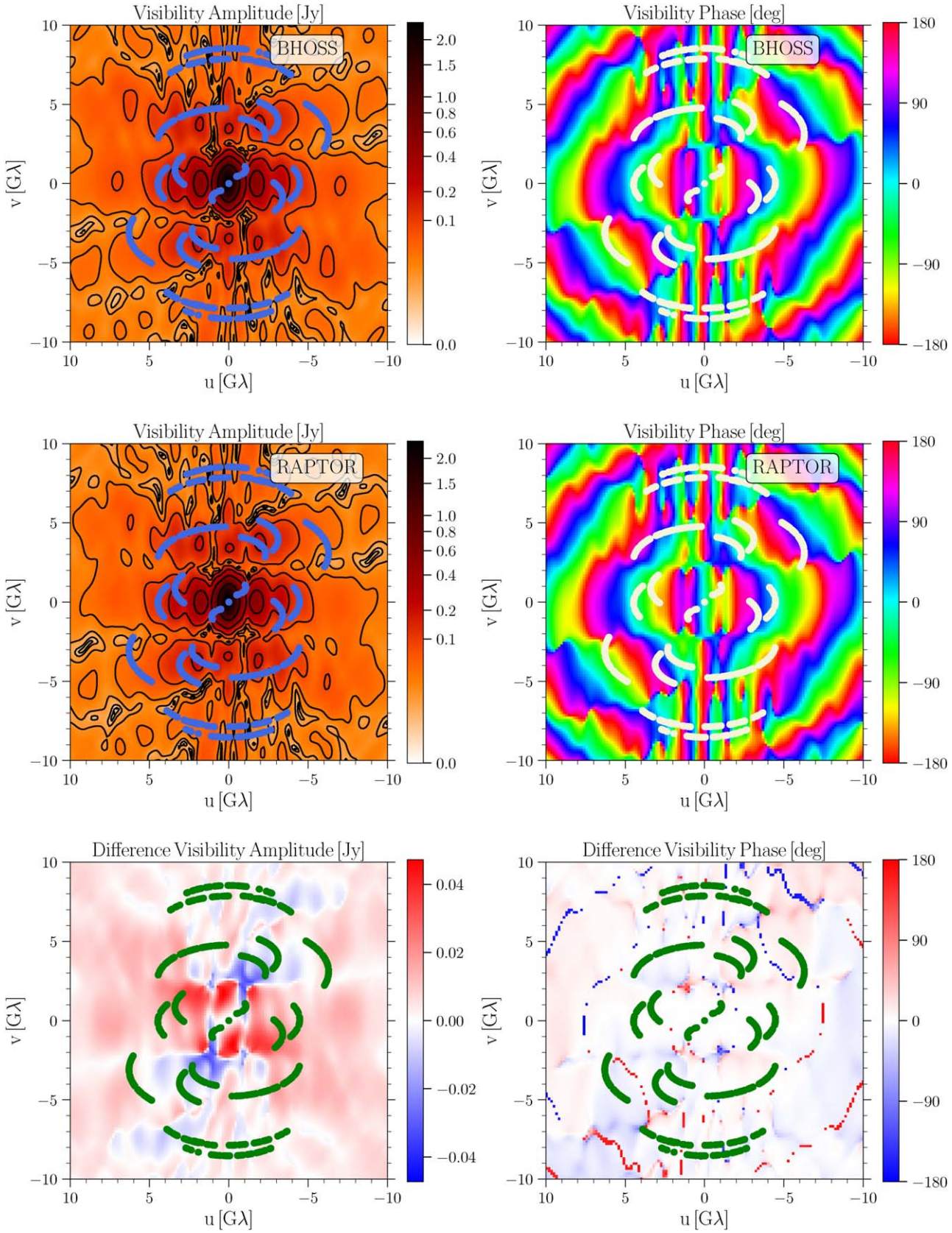

Figure 9. Intrinsic VAs and CPs for the full GRMHD comparison between BHOSS and RAPTOR. The blue dots show the *uv* coordinates probed by an EHT 2017 configuration for Sgr A*.

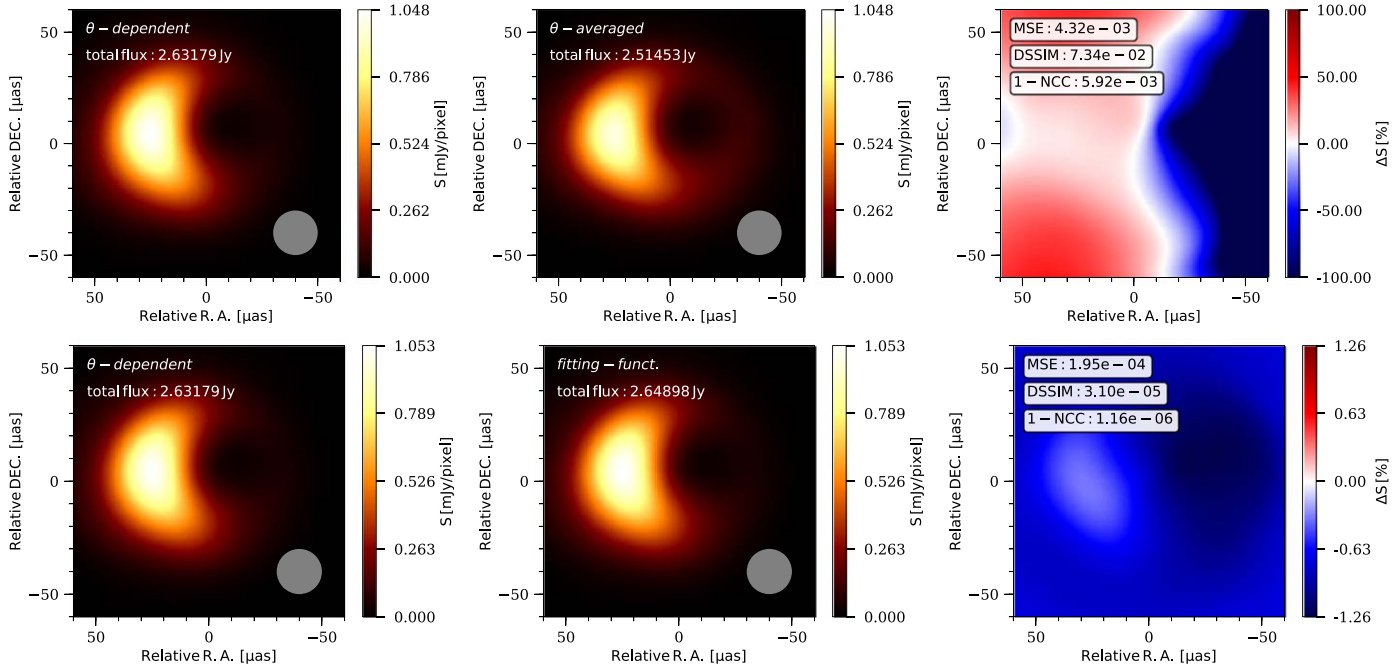

Figure 10. Model images of Sgr A* calculated with GRTRANS from a HARM GRMHD snapshot (Dexter et al. 2010). The images are convolved with a Gaussian beam (bottom right of each image). Left panels (identical): Θ-dependent emissivity from Mahadevan et al. (1996). Middle panels: Θ-averaged emissivity (upper middle from Mahadevan et al. 1996) and symphony Θ-dependent fitting function (lower middle). Right panels: difference maps between left and middle images.

from a GRMHD grid when evaluating synchrotron emissivities as well as the nontrivial influence of magnetic field distributions and temperature profiles.

The comparisons involving GRMHD-informed images also suffer from idealizing assumptions. The images from GRMHD simulations used for the comparison assume the fast-light approximation in which the GRMHD variables are held constant on the timescales that the light ray propagates through the plasma to the camera. We have also investigated a few GRMHD snapshots but note that differences arising from different snapshots or GRMHD codes are found to be substantially larger (EHT Collaboration et al. 2019d, 2019f; Porth et al. 2019) than the differences we find here. Comparisons like the one shown in Figures 8 and 9 do not include the entire budget of theoretical uncertainties. These tests assume that the correct equations are being solved and share a few common setup decisions that may not reflect all possible disparity of other radiative transfer schemes. Therefore, these comparisons, in particular the simulated data and the resulting median deviations, must be interpreted with all these caveats in mind. In other words, if the equations we are solving are the correct ones, then our ability to solve these equations is accurate enough and leads to an error that is subdominant over uncertainties arising from observations.

We stress that in generating simulated data from the models in this study we implicitly assume that the equations we solve and the physical assumptions we make are both adequate and sufficient to describe the actual physics in the astrophysical source.

Many of our physical assumptions are fairly established. However, one can identify open challenges with regards to the validity of the theoretical description for what the EHT sees and the connection to larger-scale jet structure (Chael et al. 2019; Punsly 2019; Davelaar et al. 2019). The GRMHD simulations model the matter as a single fluid that effectively describes the behavior of the protons. However, the electrons are providing most of the radiation. The current state of the art is to use phenomenological models for the electron thermodynamics, which then inform GRRT codes that produce theoretical images (EHT Collaboration et al. 2019d, 2019f). Other open questions and work beyond the current state include uncertain electron thermodynamics (Ressler et al. 2015, 2017; Chael et al. 2018), radiative cooling (Dibi et al. 2012), importance of nonthermal emission (Chael et al. 2017; Davelaar et al. 2018b, 2019), variability, and handling highly magnetized plasma (Porth et al. 2019) at low densities (i.e., nearly collisional plasmas) where the ideal MHD approximation may not hold anymore, just to name a few.

Unmodeled or incorrectly modeled physics can cause additional discrepancies and biases, which are not quantified here. The validation process necessary to make progress in this regard exceeds the scope of this work and will be tackled gradually in the future. However, for reliable model fitting and parameter estimation, the verification and comparisons of idealized and simplified cases as considered here are necessary conditions that are important to investigate.

Finally, we point out that the turbulent realizations in the model images are different from those seen in observations, and the intrinsic variability causes additional discrepancy beyond what we analyze here. This is especially true for Sgr A*, where the gravitational timescale is much shorter than the duration of an observation night.

7. Conclusions

We have assessed the accuracy of radiative transfer codes used within the EHT Collaboration via a pure ray-tracing test involving the deflection of null rays in the strongly spinning Kerr spacetime, via idealized imaging tests, and full GRMHD inspired radiative transfer models that better represent the actual application involving EHT data. This study is one of many important investigations with the ultimate goal of

arriving at a quantitative error budget of theoretical image models.

Despite the caveats mentioned in Section 6, it is expected that the tests presented here give a meaningful first measure for the level of accuracy in the ray-tracing and radiative transfer calculations performed in the EHT Collaboration. The results therefore also give a limited impression on the accuracy to be expected in the image model library, but we want to caution that any inference on the accuracy of the library needs more work. The results demonstrate that discretization errors from radiative transfer calculations are subdominant over the error budget from GRMHD simulations (Porth et al. 2019), noise due to intrinsic variability, and instrumental errors.

The typical discrepancy for practical parameter choices amounts to a deviation in total flux of about 1% for typical setups and is limited predominantly by the finite position of the camera. We find larger differences between full, pitch angle–dependent and angle-averaged synchrotron emissivity.

For each image of the various test cases and all participating radiative transfer codes, we simulated a realistic EHT observation to compute simulated VA and CP data and compared them to the corresponding simulated data for the exact solution. The result is a typical uncertainty within observational uncertainties. Our results demonstrate that provided that the physics included sufficiently captures the observed behavior, finite accuracy due to numerical error in typical radiative transfer–based model predictions is unlikely to limit the scientific predictability of the EHT for 2017 and 2018 array configurations.

Outstanding questions beyond the scope of this work, but planned for the future, include additional uncertainties such as different interpolation methods for GRMHD quantities when obtaining synchrotron emissivities, polarization (even for total intensity model image predictions), dropping the fast-light approximation, more variety in image structures from a diverse set of GRMHD simulations, different observing frequencies (especially 345 GHz), (related) different opacity regimes, variability, and alternative theories of gravity.

The authors of the present paper thank the following organizations and programs: the Academy of Finland (projects 274477, 284495, 312496); the Advanced European Network of E-infrastructures for Astronomy with the SKA (AENEAS) project, supported by the European Commission Framework Programme Horizon 2020 Research and Innovation action under grant agreement 731016; the Alexander von Humboldt Stiftung; the Black Hole Initiative at Harvard University, through a grant (60477) from the John Templeton Foundation; the China Scholarship Council; Comisión Nacional de Investigación Científica y Tecnológica (CONICYT, Chile, via PIA ACT172033, Fondecyt projects 1171506 and 3190878, BASAL AFB-170002, ALMA-conicyt 31140007); Consejo Nacional de Ciencia y Tecnología (CONACYT, Mexico, projects 104497, 275201, 279006, 281692); the Delaney Family via the Delaney Family John A. Wheeler Chair at Perimeter Institute; Dirección General de Asuntos del Personal Académico-Universidad Nacional Autónoma de México (DGAPA-UNAM, project IN112417); the European Research Council Synergy Grant "BlackHoleCam: Imaging the Event Horizon of Black Holes" (grant 610058); the Generalitat Valenciana postdoctoral grant APOSTD/2018/177 and GenT Program (project CIDEGENT/2018/021); the Gordon and Betty Moore Foundation (grants GBMF-3561, GBMF-5278); the Istituto Nazionale di Fisica Nucleare (INFN) sezione di Napoli, iniziative specifiche TEONGRAV; the International Max Planck Research School for Astronomy and Astrophysics at the Universities of Bonn and Cologne; the Jansky Fellowship program of the National Radio Astronomy Observatory (NRAO); the Japanese Government (Monbukagakusho: MEXT) Scholarship; the Japan Society for the Promotion of Science (JSPS) Grant-in-Aid for JSPS Research Fellowship (JP17J08829); the Key Research Program of Frontier Sciences, Chinese Academy of Sciences (CAS, grants QYZDJ-SSW-SLH057, QYZDJ-SSW-SYS008, ZDBS-LY-SLH011); the Leverhulme Trust Early Career Research Fellowship; the Max-Planck-Gesellschaft (MPG); the Max Planck Partner Group of the MPG and the CAS; the MEXT/JSPS KAKENHI (grants 18KK0090, JP18K13594, JP18K03656, JP18H03721, 18K03709, 18H01245, 25120007); the MIT International Science and Technology Initiatives (MISTI) Funds; the Ministry of Science and Technology (MOST) of Taiwan (105-2112-M-001-025-MY3, 106-2112-M-001-011, 106-2119-M-001-027, 107-2119-M-001-017, 107-2119-M-001-020, and 107-2119-M-110-005); the National Aeronautics and Space Administration (NASA, Fermi Guest Investigator grant 80NSSC17K0649 and Hubble Fellowship grant HST-HF2-51431.001-A awarded by the Space Telescope Science Institute, which is operated by the Association of Universities for Research in Astronomy, Inc., for NASA, under contract NAS5-26555); the National Institute of Natural Sciences (NINS) of Japan; the National Key Research and Development Program of China (grant 2016YFA0400704, 2016YFA0400702); the National Science Foundation (NSF, grants AST-0096454, AST-0352953, AST-0521233, AST-0705062, AST-0905844, AST-0922984, AST-1126433, AST-1140030, DGE-1144085, AST-1207704, AST-1207730, AST-1207752, MRI-1228509, OPP-1248097, AST-1310896, AST-1312651, AST-1337663, AST-1440254, AST-1555365, AST-1715061, AST-1615796, AST-1716327, OISE-1743747, AST-1816420); the Natural Science Foundation of China (grants 11573051, 11633006, 11650110427, 10625314, 11721303, 11725312, 11933007); the Natural Sciences and Engineering Research Council of Canada (NSERC, including a Discovery Grant and the NSERC Alexander Graham Bell Canada Graduate Scholarships-Doctoral Program); the National Youth Thousand Talents Program of China; the National Research Foundation of Korea (the Global PhD Fellowship Grant: grants NRF-2015H1A2A1033752, 2015-R1D1A1A01056807, the Korea Research Fellowship Program: NRF-2015H1D3A1066561); the Netherlands Organization for Scientific Research (NWO) VICI award (grant 639.043.513) and Spinoza Prize SPI 78–409; the New Scientific Frontiers with Precision Radio Interferometry Fellowship awarded by the South African Radio Astronomy Observatory (SARAO), which is a facility of the National Research Foundation (NRF), an agency of the Department of Science and Technology (DST) of South Africa; the Onsala Space Observatory (OSO) national infrastructure, for the provisioning of its facilities/observational support (OSO receives funding through the Swedish Research Council under grant 2017-00648); the Perimeter Institute for Theoretical Physics (research at Perimeter Institute is supported by the Government of Canada through the Department of Innovation, Science and Economic Development and by the Province of Ontario through the Ministry of

Research, Innovation and Science); the Russian Science Foundation (grant 17-12-01029); the Spanish Ministerio de Economía y Competitividad (grants AYA2015-63939-C2-1-P, AYA2016-80889-P); the State Agency for Research of the Spanish MCIU through the "Center of Excellence Severo Ochoa" award for the Instituto de Astrofísica de Andalucía (SEV-2017-0709); the Toray Science Foundation; the US Department of Energy (USDOE) through the Los Alamos National Laboratory (operated by Triad National Security, LLC, for the National Nuclear Security Administration of the USDOE (Contract 89233218CNA000001)); the Italian Ministero dell'Istruzione Università e Ricerca through the grant Progetti Premiali 2012-iALMA (CUP C52I13000140001); the European Union's Horizon 2020 research and innovation program under grant agreement No. 730562 RadioNet; ALMA North America Development Fund; the Academia Sinica; Chandra TM6-17006X; the GenT Program (Generalitat Valenciana) Project CIDEGENT/2018/021. This work used the Extreme Science and Engineering Discovery Environment (XSEDE), supported by NSF grant ACI-1548562, and CyVerse, supported by NSF grants DBI-0735191, DBI-1265383, and DBI-1743442. XSEDE Stampede2 resource at TACC was allocated through TG-AST170024 and TG-AST080026N. XSEDE JetStream resource at PTI, and TACC was allocated through AST170028. The simulations were performed in part on the SuperMUC cluster at the LRZ in Garching, on the LOEWE cluster in CSC in Frankfurt, and on the HazelHen cluster at the HLRS in Stuttgart. This research was enabled in part by support provided by Compute Ontario (http://computeontario.ca), Calcul Quebec (http://www.calculquebec.ca), and Compute Canada (http://www.computecanada.ca).

We thank the staff at the participating observatories, correlation centers, and institutions for their enthusiastic support.

This paper makes use of the following ALMA data: ADS/JAO.ALMA#2017.1.00841.V. ALMA is a partnership of the European Southern Observatory (ESO; Europe, representing its member states), NSF, and National Institutes of Natural Sciences of Japan, together with National Research Council (Canada), Ministry of Science and Technology (MOST; Taiwan), Academia Sinica Institute of Astronomy and Astrophysics (ASIAA; Taiwan), and Korea Astronomy and Space Science Institute (KASI; Republic of Korea), in cooperation with the Republic of Chile. The Joint ALMA Observatory is operated by ESO, Associated Universities, Inc. (AUI)/NRAO, and the National Astronomical Observatory of Japan (NAOJ). The NRAO is a facility of the NSF operated under cooperative agreement by AUI. APEX is a collaboration between the Max-Planck-Institut für Radioastronomie (Germany), ESO, and the Onsala Space Observatory (Sweden). The SMA is a joint project between the SAO and ASIAA and is funded by the Smithsonian Institution and the Academia Sinica. The JCMT is operated by the East Asian Observatory on behalf of the NAOJ, ASIAA, and KASI, as well as the Ministry of Finance of China, Chinese Academy of Sciences, and the National Key R&D Program (No. 2017YFA0402700) of China. Additional funding support for the JCMT is provided by the Science and Technologies Facility Council (UK) and participating universities in the UK and Canada. The LMT is a project operated by the Instituto Nacional de Astrófisica, Óptica, y Electrónica (Mexico) and the University of Massachusetts at Amherst (USA). The IRAM 30 m telescope on Pico Veleta, Spain, is operated by IRAM and supported by CNRS (Centre National de la Recherche Scientifique, France), MPG (Max-Planck-Gesellschaft, Germany), and IGN (Instituto Geográfico Nacional, Spain).

The SMT is operated by the Arizona Radio Observatory, a part of the Steward Observatory of the University of Arizona, with financial support of operations from the State of Arizona and financial support for instrumentation development from the NSF. The SPT is supported by the National Science Foundation through grant PLR-1248097. Partial support is also provided by the NSF Physics Frontier Center grant PHY-1125897 to the Kavli Institute of Cosmological Physics at the University of Chicago, the Kavli Foundation, and the Gordon and Betty Moore Foundation grant GBMF 947. The SPT hydrogen maser was provided on loan from the GLT, courtesy of ASIAA.

The EHT Collaboration has received generous donations of FPGA chips from Xilinx Inc., under the Xilinx University Program. The EHT Collaboration has benefited from technology shared under open-source license by the Collaboration for Astronomy Signal Processing and Electronics Research (CASPER). The EHT project is grateful to T4Science and Microsemi for their assistance with hydrogen masers. This research has made use of NASA's Astrophysics Data System. We gratefully acknowledge the support provided by the extended staff of the ALMA, both from the inception of the ALMA Phasing Project and through the observational campaigns of 2017 and 2018. We would like to thank A. Deller and W. Brisken for EHT-specific support with the use of DiFX. We acknowledge the significance that Maunakea, where the SMA and JCMT EHT stations are located, has for the indigenous Hawaiian people.

B.R. is supported by a Princeton/Flatiron Postdoctoral Prize Fellowship. I.M.-V. is a fellow of the GenT Program (Generalitat Valenciana) under project CIDEGENT/2018/021. A.C. was supported by NASA through the NASA Hubble Fellowship grant No. HST-HF2-51431.001-A awarded by the Space Telescope Science Institute, which is operated by the Association of Universities for Research in Astronomy, Inc., for NASA, under contract NAS5-26555.

ORCID iDs

Roman Gold https://orcid.org/0000-0003-2492-1966
Avery E. Broderick https://orcid.org/0000-0002-3351-760X
Ziri Younsi https://orcid.org/0000-0001-9283-1191
Charles F. Gammie https://orcid.org/0000-0001-7451-8935
Monika Mościbrodzka https://orcid.org/0000-0002-4661-6332
Hung-Yi Pu https://orcid.org/0000-0001-9270-8812
Thomas Bronzwaer https://orcid.org/0000-0003-1151-3971
Jordy Davelaar https://orcid.org/0000-0002-2685-2434
Jason Dexter https://orcid.org/0000-0003-3903-0373
Chi-kwan Chan https://orcid.org/0000-0001-6337-6126
Tomohisa Kawashima https://orcid.org/0000-0001-8527-0496
Yosuke Mizuno https://orcid.org/0000-0002-8131-6730
Bart Ripperda https://orcid.org/0000-0002-7301-3908
Kazunori Akiyama https://orcid.org/0000-0002-9475-4254
Antxon Alberdi https://orcid.org/0000-0002-9371-1033
Rebecca Azulay https://orcid.org/0000-0002-2200-5393

Anne-Kathrin Baczko https://orcid.org/0000-0003-3090-3975
Mislav Baloković https://orcid.org/0000-0003-0476-6647
John Barrett https://orcid.org/0000-0002-9290-0764
Lindy Blackburn https://orcid.org/0000-0002-9030-642X
Katherine L. Bouman https://orcid.org/0000-0003-0077-4367
Geoffrey C. Bower https://orcid.org/0000-0003-4056-9982
Christiaan D. Brinkerink https://orcid.org/0000-0002-2322-0749
Roger Brissenden https://orcid.org/0000-0002-2556-0894
Silke Britzen https://orcid.org/0000-0001-9240-6734
Do-Young Byun https://orcid.org/0000-0003-1157-4109
Andrew Chael https://orcid.org/0000-0003-2966-6220
Koushik Chatterjee https://orcid.org/0000-0002-2825-3590
Shami Chatterjee https://orcid.org/0000-0002-2878-1502
Ilje Cho https://orcid.org/0000-0001-6083-7521
Pierre Christian https://orcid.org/0000-0001-6820-9941
John E. Conway https://orcid.org/0000-0003-2448-9181
James M. Cordes https://orcid.org/0000-0002-4049-1882
Geoffrey B. Crew https://orcid.org/0000-0002-2079-3189
Yuzhu Cui https://orcid.org/0000-0001-6311-4345
Mariafelicia De Laurentis https://orcid.org/0000-0002-9945-682X
Roger Deane https://orcid.org/0000-0003-1027-5043
Jessica Dempsey https://orcid.org/0000-0003-1269-9667
Gregory Desvignes https://orcid.org/0000-0003-3922-4055
Sheperd S. Doeleman https://orcid.org/0000-0002-9031-0904
Ralph P. Eatough https://orcid.org/0000-0001-6196-4135
Heino Falcke https://orcid.org/0000-0002-2526-6724
Vincent L. Fish https://orcid.org/0000-0002-7128-9345
Raquel Fraga-Encinas https://orcid.org/0000-0002-5222-1361
José L. Gómez https://orcid.org/0000-0003-4190-7613
Peter Galison https://orcid.org/0000-0002-6429-3872
Boris Georgiev https://orcid.org/0000-0002-3586-6424
Minfeng Gu (顾敏峰) https://orcid.org/0000-0002-4455-6946
Mark Gurwell https://orcid.org/0000-0003-0685-3621
Kazuhiro Hada https://orcid.org/0000-0001-6906-772X
Ronald Hesper https://orcid.org/0000-0003-1918-6098
Luis C. Ho (何子山) https://orcid.org/0000-0001-6947-5846
Mareki Honma https://orcid.org/0000-0003-4058-9000
Chih-Wei L. Huang https://orcid.org/0000-0001-5641-3953
Lei Huang (黄磊) https://orcid.org/0000-0002-1923-227X
Sara Issaoun https://orcid.org/0000-0002-5297-921X
David J. James https://orcid.org/0000-0001-5160-4486
Michael Janssen https://orcid.org/0000-0001-8685-6544
Britton Jeter https://orcid.org/0000-0003-2847-1712
Wu Jiang (江悟) https://orcid.org/0000-0001-7369-3539
Michael D. Johnson https://orcid.org/0000-0002-4120-3029
Svetlana Jorstad https://orcid.org/0000-0001-6158-1708
Taehyun Jung https://orcid.org/0000-0001-7003-8643
Mansour Karami https://orcid.org/0000-0001-7387-9333
Ramesh Karuppusamy https://orcid.org/0000-0002-5307-2919
Garrett K. Keating https://orcid.org/0000-0002-3490-146X
Mark Kettenis https://orcid.org/0000-0002-6156-5617
Jae-Young Kim https://orcid.org/0000-0001-8229-7183
Junhan Kim https://orcid.org/0000-0002-4274-9373
Motoki Kino https://orcid.org/0000-0002-2709-7338
Jun Yi Koay https://orcid.org/0000-0002-7029-6658
Patrick M. Koch https://orcid.org/0000-0003-2777-5861
Shoko Koyama https://orcid.org/0000-0002-3723-3372
Michael Kramer https://orcid.org/0000-0002-4175-2271
Carsten Kramer https://orcid.org/0000-0002-4908-4925
Thomas P. Krichbaum https://orcid.org/0000-0002-4892-9586
Cheng-Yu Kuo https://orcid.org/0000-0001-6211-5581
Tod R. Lauer https://orcid.org/0000-0003-3234-7247
Sang-Sung Lee https://orcid.org/0000-0002-6269-594X
Yan-Rong Li (李彦荣) https://orcid.org/0000-0001-5841-9179
Zhiyuan Li (李志远) https://orcid.org/0000-0003-0355-6437
Rocco Lico https://orcid.org/0000-0001-7361-2460
Kuo Liu https://orcid.org/0000-0002-2953-7376
Elisabetta Liuzzo https://orcid.org/0000-0003-0995-5201
Wen-Ping Lo https://orcid.org/0000-0003-1869-2503
Laurent Loinard https://orcid.org/0000-0002-5635-3345
Ru-Sen Lu (路如森) https://orcid.org/0000-0002-7692-7967
Nicholas R. MacDonald https://orcid.org/0000-0002-6684-8691
Sera Markoff https://orcid.org/0000-0001-9564-0876
Jirong Mao (毛基荣) https://orcid.org/0000-0002-7077-7195
Daniel P. Marrone https://orcid.org/0000-0002-2367-1080
Alan P. Marscher https://orcid.org/0000-0001-7396-3332
Iván Martí-Vidal https://orcid.org/0000-0003-3708-9611
Lynn D. Matthews https://orcid.org/0000-0002-3728-8082
Lia Medeiros https://orcid.org/0000-0003-2342-6728
Karl M. Menten https://orcid.org/0000-0001-6459-0669
Izumi Mizuno https://orcid.org/0000-0002-7210-6264
James M. Moran https://orcid.org/0000-0002-3882-4414
Kotaro Moriyama https://orcid.org/0000-0003-1364-3761
Cornelia Müller https://orcid.org/0000-0002-2739-2994
Hiroshi Nagai https://orcid.org/0000-0003-0292-3645
Masanori Nakamura https://orcid.org/0000-0001-6081-2420
Neil M. Nagar https://orcid.org/0000-0001-6920-662X
Ramesh Narayan https://orcid.org/0000-0002-1919-2730
Iniyan Natarajan https://orcid.org/0000-0001-8242-4373
Roberto Neri https://orcid.org/0000-0002-7176-4046
Chunchong Ni https://orcid.org/0000-0003-1361-5699
Aristeidis Noutsos https://orcid.org/0000-0002-4151-3860
Gisela N. Ortiz-León https://orcid.org/0000-0002-2863-676X
Daniel C. M. Palumbo https://orcid.org/0000-0002-7179-3816
Jongho Park https://orcid.org/0000-0001-6558-9053
Ue-Li Pen https://orcid.org/0000-0003-2155-9578
Dominic W. Pesce https://orcid.org/0000-0002-5278-9221
Richard Plambeck https://orcid.org/0000-0001-6765-9609
Oliver Porth https://orcid.org/0000-0002-4584-2557
Jorge A. Preciado-López https://orcid.org/0000-0002-4146-0113
Dimitrios Psaltis https://orcid.org/0000-0003-4058-2837
Venkatessh Ramakrishnan https://orcid.org/0000-0002-9248-086X
Ramprasad Rao https://orcid.org/0000-0002-1407-7944
Alexander W. Raymond https://orcid.org/0000-0002-5779-4767
Luciano Rezzolla https://orcid.org/0000-0002-1330-7103
Freek Roelofs https://orcid.org/0000-0001-5461-3687
Eduardo Ros https://orcid.org/0000-0001-9503-4892
Mel Rose https://orcid.org/0000-0002-2016-8746
Alan L. Roy https://orcid.org/0000-0002-1931-0135

Chet Ruszczyk https://orcid.org/0000-0001-7278-9707
Kazi L. J. Rygl https://orcid.org/0000-0003-4146-9043
David Sánchez-Arguelles https://orcid.org/0000-0002-7344-9920
Mahito Sasada https://orcid.org/0000-0001-5946-9960
Tuomas Savolainen https://orcid.org/0000-0001-6214-1085
Lijing Shao https://orcid.org/0000-0002-1334-8853
Zhiqiang Shen (沈志强) https://orcid.org/0000-0003-3540-8746
Des Small https://orcid.org/0000-0003-3723-5404
Bong Won Sohn https://orcid.org/0000-0002-4148-8378
Jason SooHoo https://orcid.org/0000-0003-1938-0720
Paul Tiede https://orcid.org/0000-0003-3826-5648
Fumie Tazaki https://orcid.org/0000-0003-0236-0600
Remo P. J. Tilanus https://orcid.org/0000-0002-6514-553X
Michael Titus https://orcid.org/0000-0002-3423-4505
Kenji Toma https://orcid.org/0000-0002-7114-6010
Pablo Torne https://orcid.org/0000-0001-8700-6058
Thalia Traianou https://orcid.org/0000-0002-1209-6500
Sascha Trippe https://orcid.org/0000-0003-0465-1559
Huib Jan van Langevelde https://orcid.org/0000-0002-0230-5946
Ilse van Bemmel https://orcid.org/0000-0001-5473-2950
Daniel R. van Rossum https://orcid.org/0000-0001-7772-6131
John Wardle https://orcid.org/0000-0002-8960-2942
Jonathan Weintroub https://orcid.org/0000-0002-4603-5204
Robert Wharton https://orcid.org/0000-0002-7416-5209
Maciek Wielgus https://orcid.org/0000-0002-8635-4242
George N. Wong https://orcid.org/0000-0001-6952-2147
Qingwen Wu (吴庆文) https://orcid.org/0000-0003-4773-4987
Doosoo Yoon https://orcid.org/0000-0001-8694-8166
Ken Young https://orcid.org/0000-0002-3666-4920
André Young https://orcid.org/0000-0003-0000-2682
Feng Yuan (袁峰) https://orcid.org/0000-0003-3564-6437
J. Anton Zensus https://orcid.org/0000-0001-7470-3321
Guangyao Zhao https://orcid.org/0000-0002-4417-1659
Shan-Shan Zhao https://orcid.org/0000-0002-9774-3606

References

Broderick, A., & Blandford, R. 2003, MNRAS, 342, 1280
Broderick, A., & Blandford, R. 2004, MNRAS, 349, 994
Broderick, A. E., Fish, V. L., Johnson, M. D., et al. 2016, ApJ, 820, 137
Broderick, A. E., Gold, R., Karami, M., et al. 2020, ApJ, 897, 139
Broderick, A. E., Loeb, A., & Reid, M. J. 2011, ApJ, 735, 57
Bronzwaer, T., Davelaar, J., Younsi, Z., et al. 2018, A&A, 613, A2
Chael, A., Narayan, R., & Johnson, M. D. 2019, MNRAS, 486, 2873
Chael, A., Rowan, M., Narayan, R., Johnson, M., & Sironi, L. 2018, MNRAS, 478, 5209
Chael, A. A., Johnson, M. D., Narayan, R., et al. 2016, ApJ, 829, 11
Chael, A. A., Narayan, R., & Saḍowski, A. 2017, MNRAS, 470, 2367
Chan, C.-k., Medeiros, L., Özel, F., & Psaltis, D. 2018, ApJ, 867, 59
Chan, C.-k., Psaltis, D., & Özel, F. 2013, ApJ, 777, 13
Chan, C.-K., Psaltis, D., Özel, F., Narayan, R., & Saḍowski, A. 2015a, ApJ, 799, 1
Chan, C.-k., Psaltis, D., Özel, F., et al. 2015b, ApJ, 812, 103
Chatterjee, K., Liska, M., Tchekhovskoy, A., & Markoff, S. B. 2019, MNRAS, 490, 2200
Davelaar, J., Bronzwaer, T., Kok, D., et al. 2018a, ComAC, 5, 1
Davelaar, J., Mościbrodzka, M., Bronzwaer, T., & Falcke, H. 2018b, A&A, 612, A34
Davelaar, J., Olivares, H., Porth, O., et al. 2019, A&A, 632, A2
Dexter, J. 2016, MNRAS, 462, 115
Dexter, J., & Agol, E. 2009, ApJ, 696, 1616
Dexter, J., Agol, E., Fragile, P. C., & McKinney, J. C. 2010, ApJ, 717, 1092
Dibi, S., Drappeau, S., Fragile, P. C., Markoff, S., & Dexter, J. 2012, MNRAS, 426, 1928
Dolence, J. C., Gammie, C. F., Mościbrodzka, M., & Leung, P. K. 2009, ApJS, 184, 387
Event Horizon Telescope Collaboration, Akiyama, K., Alberdi, A., et al. 2019a, ApJL, 875, L1
Event Horizon Telescope Collaboration, Akiyama, K., Antxon, A., et al. 2019b, ApJL, 875, L2
Event Horizon Telescope Collaboration, Akiyama, K., Alberdi, A., et al. 2019c, ApJL, 875, L3
Event Horizon Telescope Collaboration, Akiyama, K., Alberdi, A., et al. 2019d, ApJL, 875, L4
Event Horizon Telescope Collaboration, Akiyama, K., Alberdi, A., et al. 2019e, ApJL, 875, L5
Event Horizon Telescope Collaboration, Akiyama, K., Alberdi, A., et al. 2019f, ApJL, 875, L6
Fuerst, S. V., & Wu, K. 2004, A&A, 424, 733
Gammie, C. F., McKinney, J. C., & Tóth, G. 2003, ApJ, 589, 444
Gralla, S. E., & Lupsasca, A. 2020, PhRvD, 101, 044032
Hindmarsch, A. 2007, in Scientific Computing, ed. R. S. Stepleman et al. (Amsterdam: North-Holland), 55
Iyer, S. V., & Hansen, E. C. 2009, PhRvD, 80, 124023
Kawashima, T., Kino, M., & Akiyama, K. 2019, ApJ, 878, 27
Landi Degl'Innocenti, E. 1985, SoPh, 102, 1
Leung, P. K., Gammie, C. F., & Noble, S. C. 2011, ApJ, 737, 21
Liska, M., Hesp, C., Tchekhovskoy, A., et al. 2018, MNRAS, 474, L81
Lu, R.-S., Roelofs, F., Fish, V. L., et al. 2016, ApJ, 817, 173
Mahadevan, R., Narayan, R., & Yi, I. 1996, ApJ, 465, 327
Mihalas, D., & Mihalas, B. W. 1984, Foundations of Radiation Hydrodynamics (New York: Oxford Univ. Press)
Mizuno, Y., Younsi, Z., Fromm, C. M., et al. 2018, NatAs, 2, 585
Mościbrodzka, M., Falcke, H., & Shiokawa, H. 2016, A&A, 586, A38
Mościbrodzka, M., & Gammie, C. F. 2018, MNRAS, 475, 43
Nalewajko, K., Sikora, M., & Różańska, A. 2020, A&A, 634, A38
Noble, S. C., Gammie, C. F., McKinney, J. C., & del Zanna, L. 2006, ApJ, 641, 626
Noble, S. C., Krolik, J. H., & Hawley, J. F. 2009, ApJ, 692, 411
Noble, S. C., Leung, P. K., Gammie, C. F., & Book, L. G. 2007, CQGra, 24, S259
Pandya, A., Zhang, Z., Chandra, M., & Gammie, C. F. 2016, ApJ, 822, 34
Porth, O., Olivares, H., Mizuno, Y., et al. 2017, ComAC, 4, 1
Porth, O., Chatterjee, K., Narayan, R., et al. 2019, ApJS, 243, 26
Pu, H.-Y., Akiyama, K., & Asada, K. 2016a, ApJ, 831, 4
Pu, H.-Y., & Broderick, A. E. 2018, ApJ, 863, 148
Pu, H.-Y., Yun, K., Younsi, Z., & Yoon, S.-J. 2016b, ApJ, 820, 105
Punsly, B. 2019, ApJL, 879, L11
Rees, D. E., Murphy, G. A., & Durrant, C. J. 1989, ApJ, 339, 1093
Ressler, S. M., Tchekhovskoy, A., Quataert, E., & Gammie, C. F. 2017, MNRAS, 467, 3604
Ressler, S. M., Tchekhovskoy, A., Quataert, E., Chandra, M., & Gammie, C. F. 2015, MNRAS, 454, 1848
Rybicki, G. B., & Lightman, A. P. 2004, Radiative Processes in Astrophysics (New York: Wiley-VCH)
Thompson, C., Blandford, R. D., Evans, C. R., & Phinney, E. S. 1994, ApJ, 422, 304
Younsi, Z., Porth, O., Mizuno, Y., Fromm, C. M., & Olivares, H. 2020, in IAU Symp. 342, Perseus in Sicily: From Black Hole to Cluster Outskirts (Cambridge: Cambridge Univ. Press), 9
Younsi, Z., Wu, K., & Fuerst, S. V. 2012, A&A, 545, A13
Younsi, Z., Zhidenko, A., Rezzolla, L., Konoplya, R., & Mizuno, Y. 2016, PhRvD, 94, 084025
Yuan, F., & Narayan, R. 2014, ARA&A, 52, 529